Cell Reports

Article

Tumor eradication by hetIL-15 locoregional therapy correlates with an induced intratumoral CD103^{int}CD11b^{+} dendritic cell population

Graphical abstract

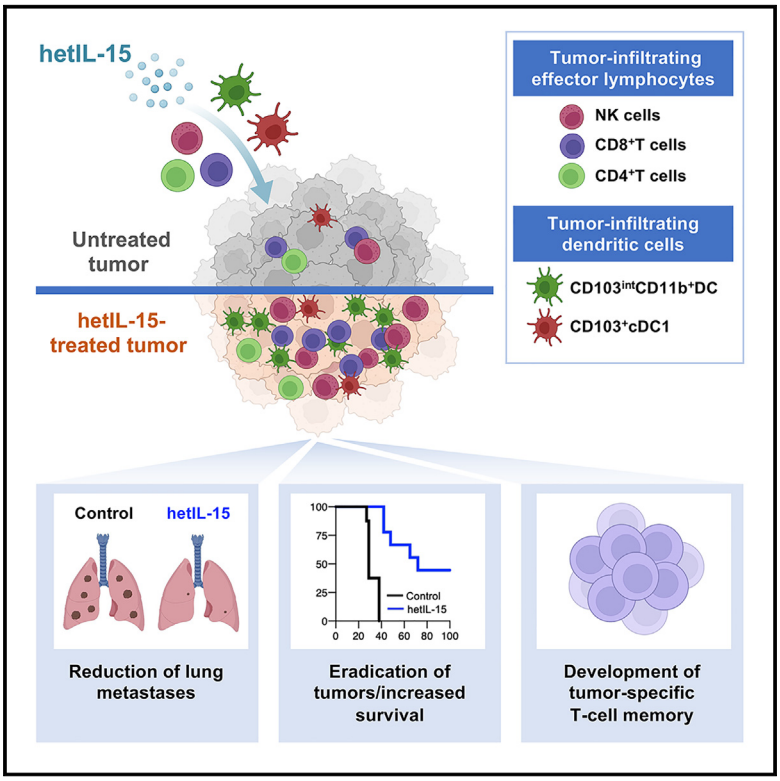

Highlights

- hetIL-15 locoregional administration eradicates EO771 tumors
- Locoregional hetIL-15 results in long-lasting specific anti-tumor immunity
- hetIL-15 induces a distinct CD103^{int}CD11b^{+} DC population in TNBC tumor models
- Transcriptional signature of CD103^{int}CD11b^{+}DCs is similar to monocyte-derived DCs

Authors

Dimitris Stellas, Sevasti Karaliota, Vasiliki Stravokefalou, ..., Cristina Bergamaschi, Barbara K. Felber, George N. Pavlakis

Correspondence

george.pavlakis@nih.gov (G.N.P.), dstellas@eie.gr (D.S.)

In brief

Stellas et al. show that hetIL-15 monotherapy orchestrates an interplay between lymphoid and myeloid immune cells leading to the tumor infiltration of cytotoxic lymphocytes, cDC1s, and of a distinct CD103^{int}CD11b^{+} DC subpopulation and resulting in eradication of TNBC tumors in mice, with generation of long-term immunological memory.

Stellas et al., 2023, Cell Reports *42*, 112501
May 30, 2023
https://doi.org/10.1016/j.celrep.2023.112501

CellPress

Cell Reports

CellPress
OPEN ACCESS

Article

Tumor eradication by hetIL-15 locoregional therapy correlates with an induced intratumoral CD103^{int}CD11b^{+} dendritic cell population

Dimitris Stellas,[1,2,9,*] Sevasti Karaliota,[1,3,9] Vasiliki Stravokefalou,[1,4] Matthew Angel,[5,6] Bethany A. Nagy,[7] Katherine C. Goldfarbmuren,[5,6] Cristina Bergamaschi,[8] Barbara K. Felber,[8] and George N. Pavlakis[1,10,*]

[1]Human Retrovirus Section, Vaccine Branch, Center for Cancer Research, National Cancer Institute at Frederick, Frederick, MD 21702, USA
[2]Department of Chemical Biology, National Hellenic Research Foundation, 11635 Athens, Greece
[3]Basic Science Program, Frederick National Laboratory for Cancer Research, Leidos Biomedical Research, Inc., Frederick, MD 21702, USA
[4]Department of Pharmacology, Faculty of Medicine, University of Thessaly, 41500 Larissa, Greece
[5]Vaccine Branch, Center for Cancer Research, National Cancer Institute, Bethesda, MD 20892, USA
[6]Advanced Biomedical Computational Science, Frederick National Laboratory for Cancer Research, Leidos Biomedical Research, Inc., Frederick, MD 21702, USA
[7]Laboratory Animal Sciences Program, Frederick National Laboratory for Cancer Research, Leidos Biomedical Research, Inc., Frederick, MD 21702, USA
[8]Human Retrovirus Pathogenesis Section, Vaccine Branch, Center for Cancer Research, National Cancer Institute at Frederick, Frederick, MD 21702, USA
[9]These authors contributed equally
[10]Lead contact
*Correspondence: george.pavlakis@nih.gov (G.N.P.), dstellas@eie.gr (D.S.)
https://doi.org/10.1016/j.celrep.2023.112501

SUMMARY

Locoregional monotherapy with heterodimeric interleukin (IL)-15 (hetIL-15) in a triple-negative breast cancer (TNBC) orthotopic mouse model resulted in tumor eradication in 40% of treated mice, reduction of metastasis, and induction of immunological memory against breast cancer cells. hetIL-15 re-shaped the tumor microenvironment by promoting the intratumoral accumulation of cytotoxic lymphocytes, conventional type 1 dendritic cells (cDC1s), and a dendritic cell (DC) population expressing both CD103 and CD11b markers. These CD103^{int}CD11b^{+}DCs share phenotypic and gene expression characteristics with both cDC1s and cDC2s, have transcriptomic profiles more similar to monocyte-derived DCs (moDCs), and correlate with tumor regression. Therefore, hetIL-15, a cytokine directly affecting lymphocytes and inducing cytotoxic cells, also has an indirect rapid and significant effect on the recruitment of myeloid cells, initiating a cascade for tumor elimination through innate and adoptive immune mechanisms. The intratumoral CD103^{int}CD11b^{+}DC population induced by hetIL-15 may be targeted for the development of additional cancer immunotherapy approaches.

INTRODUCTION

Triple-negative breast cancer (TNBC) accounts for 10%–20% of all breast cancer cases, is highly metastatic, and is associated with poor prognosis and survival.[1,2] Chemotherapy remains the standard of care for the TNBC. Immunotherapy has emerged as a promising treatment option for many cancer types and is rapidly being adopted in the clinic. The US Food and Drug Administration (FDA) has approved chemo-immunotherapy combinations (atezolizumab or pembrolizumab) for the treatment of TNBC, showing that immunotherapy can be effective in breast cancer.[3] The presence of tumor-infiltrating lymphocytes (TILs), especially CD8^{+} cytotoxic T cells, is widely recognized as a predictor of good prognosis in TNBC.[4,5] Additionally, peripheral granulocytic and monocytic expansion as well as impaired differentiation and reduction of conventional type 1 dendritic cells (cDC1s) are hallmarks of tumor progression.[6,7] In surgical specimens from patients with TNBC tumors, the presence of CD11c^{+} dendritic cells (DCs) significantly correlated with CD4^{+} and CD8^{+} T cell counts and TIL levels.[8]

cDC1s, cDC2s, and plasmacytoid DCs (pDCs) are defined by expression of cell surface markers and develop from well-known common DC and pre-cDC progenitors through the action of lineage-defining transcription factors.[9–12] Interferon regulatory factor 8 (IRF8) and Batf3 drive the development of chemokine receptor XCR1-expressing cDC1s, which have the capacity to present and cross-present antigens to CD8^{+} T cells. On the other hand, IRF4 drives the development and terminal differentiation of the CD11b^{+}CD172a^{+}-expressing cDC2 lineage, which is more specialized in polarizing CD4^{+}T helper (Th) cell responses.[13–15] Moreover, upon development of tissue inflammation, Ly6C^{hi}CD11b^{+}CD172a^{+} monocytes enter antigen-exposed barrier sites

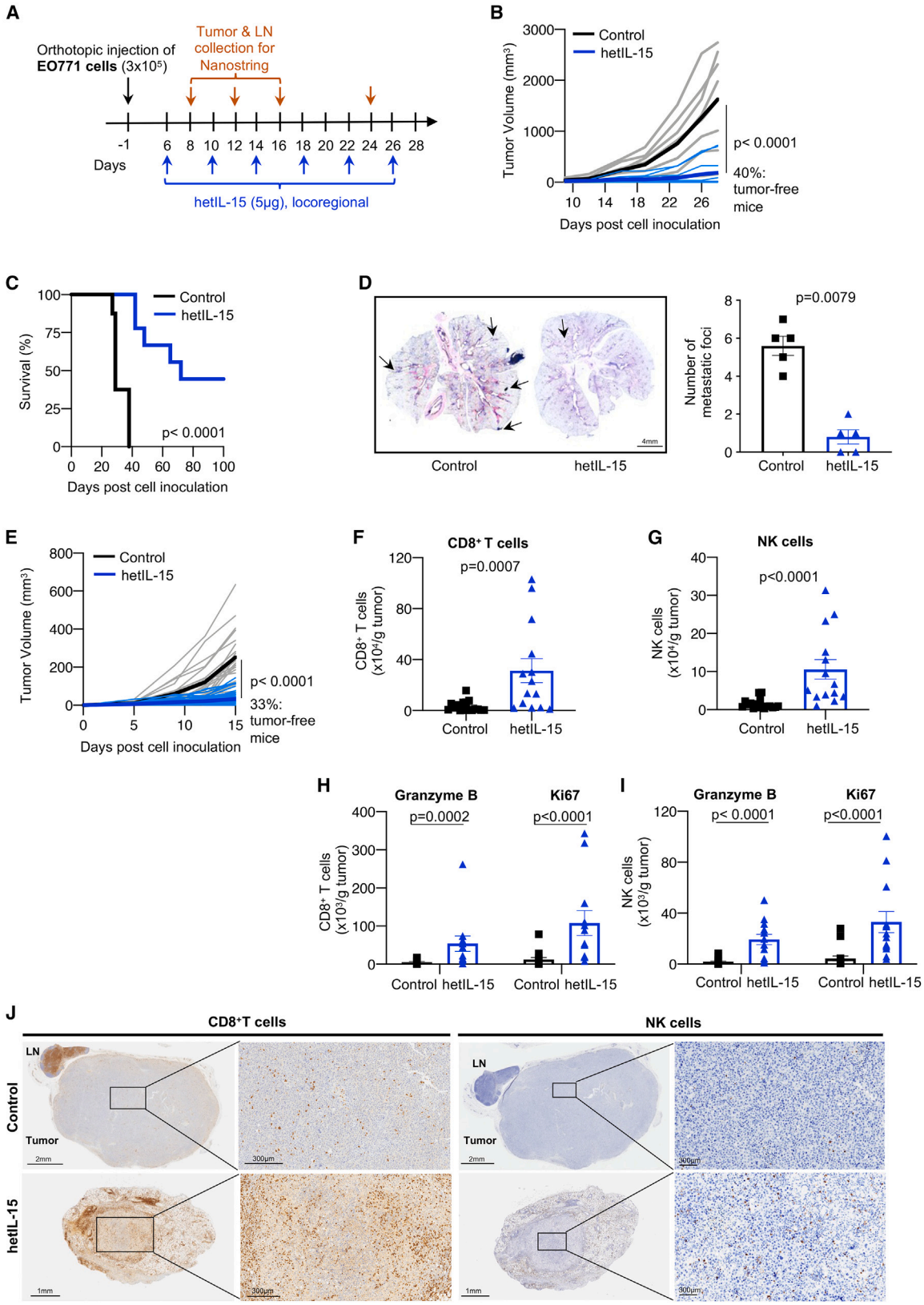

(legend on next page)

and lymph nodes (LNs). Monocytes can then rapidly upregulate the expression of major histocompatibility complex class II (MHCII) and CD11c while downregulating expression of Ly6C. These cells, known as monocyte-derived DCs (moDCs),[16,17] perform well in *ex vivo* antigen-presentation assays, leading to their classification as professional antigen-presenting cells (APCs).[18–20]

The interplay between the cancer cells and the immune system is regulated by the secretion of many different cytokines and chemokines, which shape the microenvironment and often are predictors of successful treatment. Interleukin-15 (IL-15), a homeostatic cytokine belonging to the gamma-chain family of cytokines,[21–23] has been shown to regulate a wide range of immune functions, including development of natural killer (NK) cells and the maintenance of memory T cells. IL-15 is also capable of enhancing the *in vivo* anti-tumor activity of adoptively transferred, tumor-reactive $CD8^+$ T cells and promotes infiltration and proliferation of adoptively transferred cells specifically in the tumor in an antigen-specific way.[24–27] IL-15 has shown anti-cancer activity in many preclinical model systems[28–32] and is presently being tested in multiple clinical trials for cancer immunotherapy.[33–39]

We have previously shown that bioactive IL-15 *in vivo* comprises a complex of the IL-15 polypeptide chain with the IL-15 receptor alpha chain that are together named heterodimeric IL-15 (hetIL-15).[40,41] This heterodimer is either cell associated or in a soluble form, freely circulating in blood.[42,43] In this study, we investigated the effect of hetIL-15 monotherapy after locoregional administration in orthotopically implanted murine TNBC tumors. We identified hetIL-15-triggered interactions between tumor-infiltrating lymphoid and myeloid cells and characterized a previously not recognized population of tumor-infiltrating DCs, which is increased upon hetIL-15 administration and correlated with the anti-tumoral immune responses, the generation of anti-tumoral memory, and the disease outcome, eliminating both the primary and the metastatic tumors.

RESULTS

hetIL-15 locoregional administration eradicates EO771 tumors

To evaluate the anti-cancer effect of hetIL-15-based immunotherapy, we used the EO771 model of TNBC. We performed orthotopic inoculation of EO771 cancer cells in the fourth mammary fat pad of C57BL/6 mice. Treatment was initiated when tumors reached ~20 mm^3,and hetIL-15 was provided every 4 days locoregionally (in proximity to the tumor) at a dose of 5μg/injection. Three to six injections of the cytokine or the formulation without the cytokine were given in different experiments (Figure 1A). Groups of animals were analyzed at different times as detailed in figure legend to determine the effects of hetIL-15 in tumor growth, overall survival, and metastatic disease. Six injections completely eradicated the tumors in 40% of hetIL-15-treated mice (Figure 1B) and increased survival (Figure 1C). The animals did not develop tumor regrowth or signs of morbidity that could implicate metastatic disease. Further support of this anti-metastatic action was provided by examining the lungs of the hetIL-15-treated mice, a frequent metastatic site for these tumors. The lungs revealed significant reduction in the number of metastatic foci, as was shown by H&E histological analysis (Figure 1D), supporting a beneficial role of hetIL-15 also in the control of metastatic burden.

EO771 tumors were analyzed by flow cytometry and immunohistochemistry (IHC) to explore the changes in the tumor immune phenotype upon hetIL-15 treatment. The shorter treatment schedule consisting of three hetIL-15 injections was used for these analyses, and the tumors were assessed 48 h after the last injection (Figure 1A). Flow cytometric analysis revealed significant accumulation of both $CD8^+$ T and NK cells (Figures 1F and 1G) in the hetIL-15-treated tumors. The tumor-infiltrating $CD8^+$ T and NK cells were characterized by higher content of the cytotoxic marker granzyme B and increased proliferation, as evaluated by the expression of Ki67 (Figures 1H and 1I). Furthermore, IHC analysis verified these results, showing increased accumulation of $CD8^+$ T and NK cells (Figure 1J) in the hetIL-15-treated tumors. Overall, hetIL-15 administration altered the tumor microenvironment by promoting the intratumoral infiltration of activated cytotoxic T and NK cells, as we previously reported.[24,28]

To better understand the contribution of the innate and adaptive immunity in hetIL-15-anti-tumor effect, we evaluated the treatment using *Rag-1* knockout (ko) (Figures S1A and S1B) and NK cell-depleted C57BL/6 mice (Figures S1C and S1D). Six hetIL-15 injections resulted in significant tumor growth delay

Figure 1. hetIL-15 administration resulted in significant EO771 tumor growth delay or eradication and increased survival

(A) Treatment timeline. On day −1, C57BL/6 mice were inoculated with 3×10^5 EO771 cells orthotopically in the fourth mammary pad. Mice with palpable tumors were distributed in different groups 7 days later and treated locoregionally with hetIL-15 injections (5 μg/dose/mouse) in the mammary fat pad in the vicinity of the tumor every 4 days. Three to six injections were delivered in different experiments. Orange arrows indicate days of tumor and draining LNs collection.

(B) Tumor growth curves of EO771 tumor-bearing C57BL/6 mice treated with six hetIL-15 doses (5 μg/dose/mouse) or vehicle (control) every 4 days. Data shown are from one experiment with eight or nine mice per group. Bold lines indicate average values.

(C) Kaplan-Meier survival curve of EO771 tumor-bearing C57BL/6 mice of the experiment in (B). Surviving mice resisted rechallenge (see Figure 7). Statistical significance was calculated using the log rank (Mantel-Cox) test.

(D) H&E representative staining images of EO771 lung metastases in control or hetIL-15-treated C57BL/6 mice. hetIL-15 (5 μg/dose/mouse) was injected every 4 days for a total of five doses. Data in graph represented as mean ± SEM are from one experiment with five mice per group.

(E) Tumor growth over time in three short-term independent experiments combined. Control mice (n = 21) and hetIL-15-treated mice (n = 54) received three injections (5 μg/dose/mouse) every 4 days, starting at day 6.

(F–I) Tumor immune cell infiltrates were analyzed by flow cytometry to determine absolute numbers of cells per gram of tissue: $CD8^+$ T (F), NK (G), granzyme B^+ and $Ki67^+CD8^+$ T (H), or granzyme B^+ and $Ki67^+$ NK (I) cells. Data of three independent experiments with four to six mice per group were combined; bars represent mean ± SEM. Each symbol refers to one mouse.

(J) EO771 tumor sections from mice treated with three injections of hetIL-15 or vehicle (control), as indicated. TILs were identified by immunohistochemical staining using antibodies specific for $CD8^+$ or NK.1.1 cells. A representative image from one mouse/group is shown. For (F)–(J), analysis was conducted 48 h post-third hetIL-15 injection. For (B) and (E), statistical significance was calculated by mixed-effects analysis and for (D) and (F)–(I) by Mann-Whitney U test.

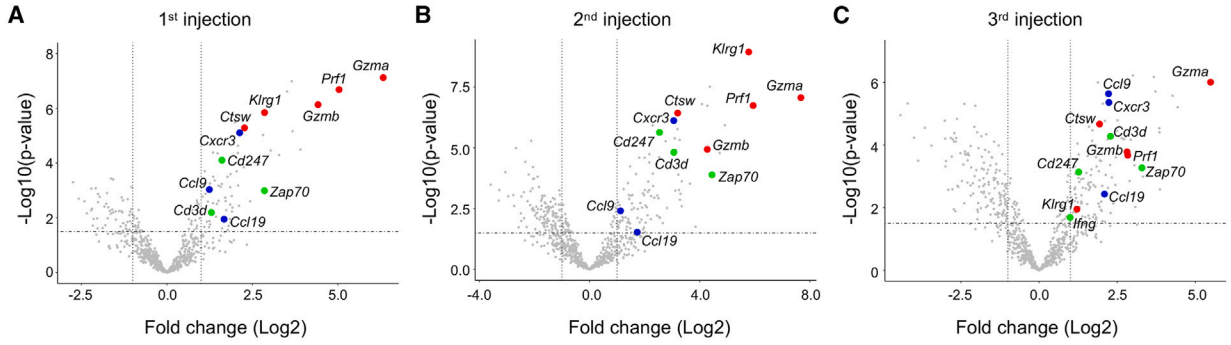

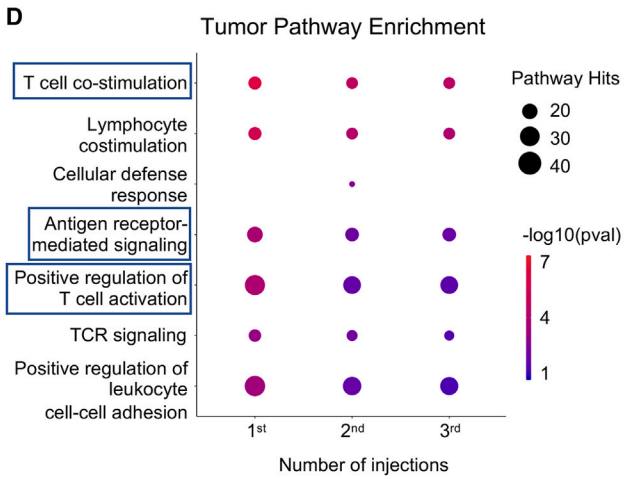

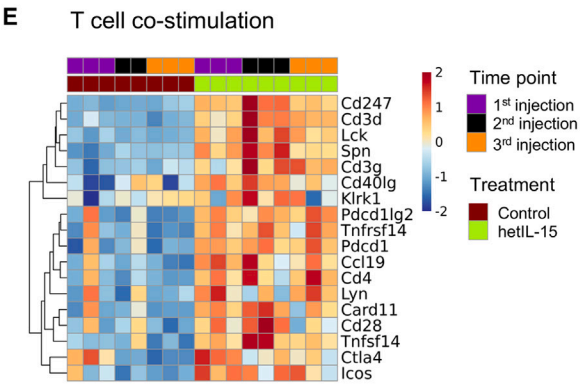

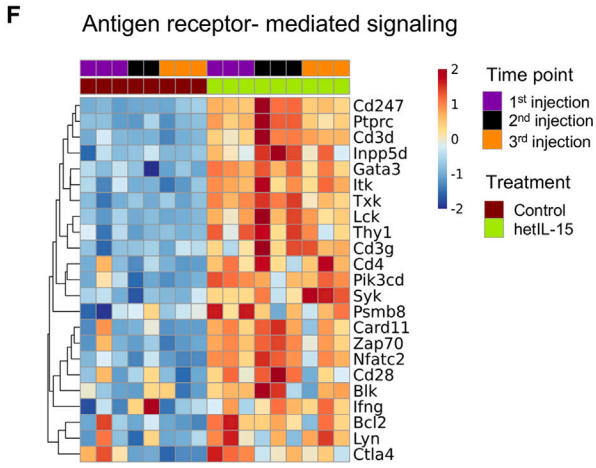

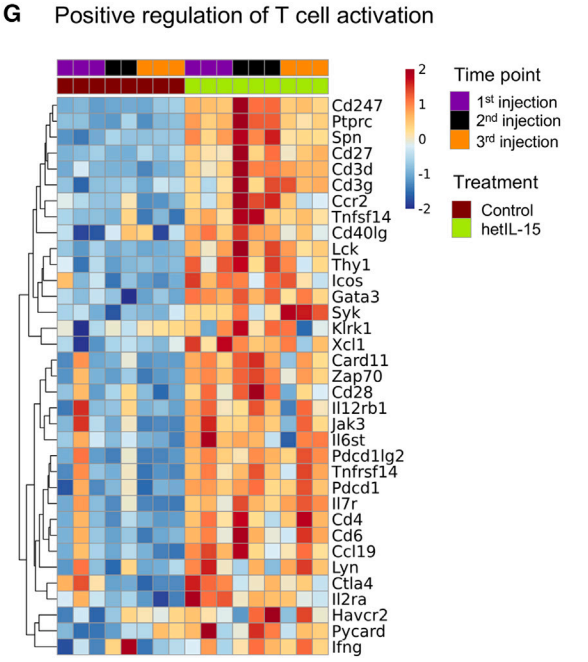

(legend on next page)

compared with the control group in *Rag-1* ko mice, but none of them achieved complete tumor regression (Figure S1A). In contrast, treatment with the same number of hetIL-15 injections in NK cell-depleted mice resulted in 20% complete tumor regression and significant tumor growth control in the rest of the animals (Figure S1C). Beneficial effects of hetIL-15 treatment on metastatic burden were observed in both *Rag-1* ko (Figure S1B) and NK cell-depleted mice (Figure S1D). Thus, both T and NK cells contributed to the anti-tumor effect of hetIL-15 on tumor growth delay and metastatic disease in the EO771 model; however, tumor eradication required the presence of T cells.

hetIL-15 treatment enhanced the intratumoral expression of genes associated with lymphocyte migration, activation, and cytotoxicity

To gain more detailed understanding of the function of TILs, we performed gene expression analysis of EO771 tumors excised 48 h after either the first, second, or third hetIL-15 administration (treatment schedule, Figure 1A), using a panel of 770 immune-oncology related gene probes (NanoString Technologies). We identified ~300 differentially expressed genes (log2 fold change > 1, adjusted $p < 0.05$) in tumors from hetIL-15-treated mice compared with control animals at all three analyzed time points (Figures 2A–2C). Genes associated with a cytotoxic phenotype, such as *Gzmb*, *Gzma*, *Prf1*, *Ctsw*, and *Klrg1* (red dots), were among the most significantly overexpressed genes in hetIL-15-treated mice (Figures 2A–2C). In addition, expression of *Zap70*, *Cd247*, *Cd3d*, and *Ifng* (green dots), as well as *Cxcr3*, *Ccl9*, and *Ccl19* (blue dots), was also increased, highlighting the stimulation of pathways related to T cell activation/T cell receptor (TCR) signaling and leukocyte migration. Gene Ontology (GO) pathway enrichment analysis of the NanoString data showed that the T cell co-stimulation (GO: 0031295), the antigen receptor-mediated signaling (GO: 0050851), and the positive regulation of T cell activation (GO: 0050870) pathways ranked in the top 10 canonical pathways upregulated upon hetIL-15 treatment (Figure 2D). The upregulated genes that are associated with these pathways are depicted in Figures 2E–2G.

To analyze the systemic effects of locoregional hetIL-15 treatment, we also evaluated the gene expression pattern in draining LNs (dLNs) 48 h after the first, second, or third hetIL-15 injection. Transcriptomic analysis of the dLNs (Figures S2A–S2C) further supported the findings that hetIL-15 enhanced T cell cytotoxicity (*Gzmb*, *Gzma*, *Prf1*, *Ctswi*, and *Klrg1*), TCR activation (*Zap70* and *Ifng*), and chemotaxis of immune cell chemotaxis (*Cxcr3*, *Ccr5*, *Cxcl9*, and *Ccl9*). GO pathway enrichment analysis revealed that leukocyte migration (GO: 0050900, p = 0.03; second injection, p = 0.01; third injection) and T cell activation (GO: 0002286, p = 0.0015; second injection) ranked among the top upregulated canonical pathways (Figures S2D and S2E). Flow cytometric analysis of dLNs also showed an increased frequency of $CD8^+$ T and NK cells (Figures S2F and S2G). Overall, these data demonstrate that hetIL-15 induced a cascade of transcriptional events triggering the cytotoxic capacity and activation of T and NK cells as well as their accumulation within the tumors and dLNs.

hetIL-15 locoregional administration induced the accumulation of a distinct DC population, $CD103^{int}CD11b^+$ DC, in different breast cancer models

Our initial transcriptomic data analysis showed that hetIL-15 treatment also affected the myeloid cell composition of the tumors. hetIL-15 monotherapy was associated with a significant upregulation of the gene expression profile of cytotoxic cells, NK, $CD8^+$ T, Th1 cells, macrophages, and DCs (Figure 3A). Guided by our transcriptomic data and our recent report from Bergamaschi et al.,[28] we established a flow cytometry staining protocol (Figure 3B) that allows distinction of different myeloid cell populations.[11,44] $CD103^+$cDC1s were defined as Lin(NK 1.1,CD19,B220,CD3)$^{neg}CD64^-MHCII^+CD11c^+$ $CD103^+CD11b^-$; $CD11b^+$cDC2s were defined as Lin(NK1.1,CD19,B220,CD 3)$^{neg}CD64^-$ $MHCII^+CD11c^+CD103^-CD11b^+$, and macrophages were defined as Lin(NK1.1, CD19,B220,CD3)^{neg} $CD64^+F4/80^+$. Locoregional hetIL-15 treatment resulted in increased tumor infiltration of $CD103^+$cDC1s (Figure 3C), whereas no statistical significant difference was found in the number of $CD11b^+$ cDC2s (Figure 3D). Surprisingly, flow cytometry analysis revealed an additional DC population that was distinct from the DC subsets previously reported in tumor mouse models. This DC population, referred to as $CD103^{int}CD11b^+$DC, shows a unique phenotypic expression of the CD103 and CD11b markers (Figure 3B). This population represented a minority of $MHCII^+$ $CD11c^+$ cells in the untreated tumors but became the most prominent $MHCII^+CD11c^+$ population in tumors upon hetIL-15 treatment (Figure 3E). Importantly, tumor infiltration by both $CD103^+$cDC1s and $CD103^{int}CD11b^+$DCs inversely correlated with the EO771 tumor size in hetIL-15-treated animals 48 h after the third hetIL-15 injection (Figure 3F). In contrast, no correlation between intratumoral $CD11b^+$cDC2s and tumor size was observed (Figure 3F). In addition, flow cytometric analysis of the tumor-infiltrating DC populations 48 h after the first, second, and third hetIL-15 injection was performed (Figures S3A–S3C). This analysis showed that tumor-infiltrating $CD103^+$cDC1s (Figure S3A) were increased in the hetIL-15-treated mice, compared

Figure 2. Transcriptomic analysis of hetIL-15-treated tumors revealed an activated tumor-infiltrating immune cell profile

Gene expression analysis of EO771 tumors recovered from mice treated with either PBS (n = 3) or hetIL-15 (5 μg/dose/mouse every 4 days) (n = 2–3) was performed by the NanoString Technologies using a panel of 770 immune-oncology related gene probes (PanCancer Immune Profiling Panel). The analysis was conducted 48 h post-first, -second, and -third hetIL-15 injection.

(A–C) Volcano plots depict differentially expressed genes between the two treatment groups after the first (A), second (B), and third (C) hetIL-15 dose. The genes marked in red, green, and blue are associated with T and NK cell cytotoxicity, enhanced T cell activation/TCR signaling, and lymphocyte migration, respectively. Dashed line represents Benjamini-Hochberg adjusted p value = 0.05 and dotted lines represent log2(FC) = 1 and log2(FC) = −1.

(D) GO tumor-enriched pathways from differentially expressed genes are presented.

(E–G) Heatmaps of expressed genes in pathways of T cell co-stimulation (E), antigen receptor-mediated signaling (F), and positive regulation of T cell activation (G) show the upregulated genes in hetIL-15-treated tumors compared with control tumors.

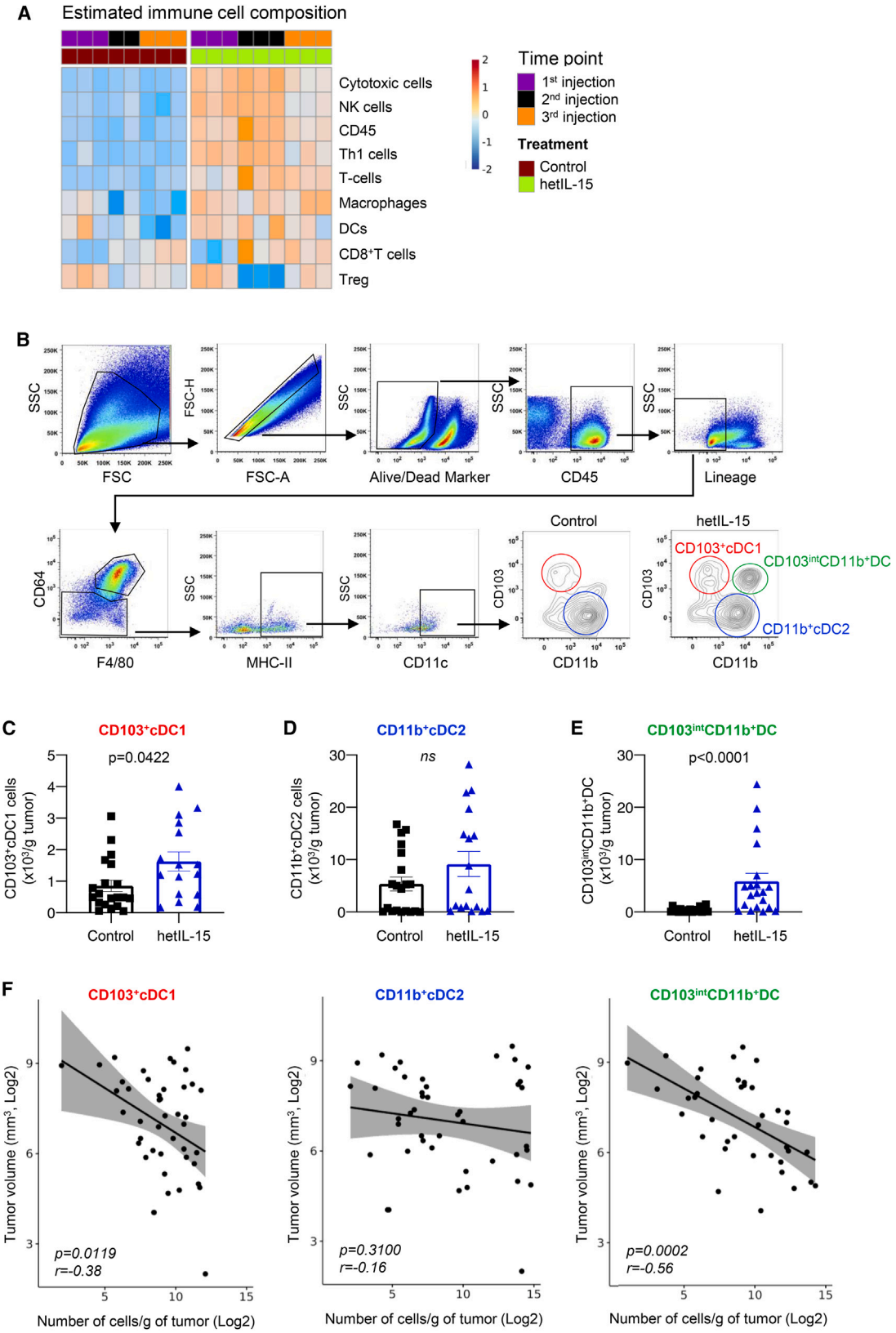

(legend on next page)

with control mice, 48 h after the second hetIL-15 injection. In contrast, CD11b$^+$cDC2s (Figure S3B) and especially the CD103^{int}CD11b$^+$DC (Figure S3C) were present in the tumors of hetIL-15-treated mice in higher numbers as early as 48 h after the first hetIL-15 injection; administration of hetIL-15 preserved their number until the end of the treatment period. To study the potential contribution of NK cells in the generation of the CD103^{int}CD11b$^+$DC population in combination with the hetIL-15-anti-tumor effect, we evaluated treatment by hetIL-15 using NK cell-depleted C57BL/6 mice (Figures S3D–S3E). Antibody-mediated depletion of NK cells in C57BL/6 mice resulted in a rapid growth of EO771 tumors (Figure S3D) in untreated mice and a decrease in the CD103^{int}CD11b$^+$DC population within the hetIL-15-treated tumors 48 h after the first hetIL-15 injection (Figure S3E), suggesting that CD103^{int}CD11b$^+$DCs accumulation depended on NK cells.

The t-distributed stochastic neighbor embedding (t-SNE) analysis from six control and five hetIL-15-treated-concatenated tumors revealed that the different DC subtypes formed unique distinct clusters (i.e., CD103$^+$cDC1, CD11b$^+$cDC2, CD103^{int}CD11b$^+$DC; Figure 4A). Phenotypic profiling of the CD103^{int}CD11b$^+$DCs in hetIL-15-treated tumors revealed that the cells expressed strongly and uniformly the DC marker CD24,[11] while they lacked expression of the macrophage markers CD64 (Fcgr1), CD169, CX3CR1, and Ly6C (Figures 4B and 4C), with the exception of the F4/80 marker (Figure 4D), suggesting they were not of macrophage lineage. *CD24a* was absent on macrophages but significantly expressed on DCs[11,45] and on moDC populations.[46] The CD24a role has been associated with promoting the differentiation of naive CD8$^+$ T cells into effector or memory CD8$^+$ T cells.[47] Tumor-infiltrating CD103^{int}CD11b$^+$ DCs were also characterized by intermediate expression of XCR1 and IRF8 (Figure 4E). Moreover, CD103^{int}CD11b$^+$ DCs were positive for the TREM1 and CD101 markers, compared with the cDC1s and cDC2s (Figure 4F), showing similarities with a population of CD103$^+$CD11b$^+$DCs found only in the intestinal lamina propria.[48,49]

We confirmed our results in an additional TNBC mouse model, 4T1, which is syngeneic to Balb/c mice. After orthotopic implantation of 4T1 cells in Balb/c mice and the establishment of the tumors, the mice were treated locoregionally with three hetIL-15 injections (Figure S4A). hetIL-15 treatment resulted in a significant decrease of the primary tumor volume (Figure S4B). Flow cytometric analysis of TILs showed increased infiltration of both CD8$^+$ T and NK cells (Figures S4C and S4D). Upon hetIL-15 treatment, CD103$^+$cDC1s were not affected by hetIL-15 in this model, in contrast to CD11b$^+$cDC2s, which were significantly increased (Figures S4E and S4F). Importantly, the CD103^{int}CD11b$^+$DCs were found to be accumulated intratumorally upon hetIL-15 treatment (Figure S4G). Verifying the previous results of the EO771 tumor model, the 4T1 tumor-infiltrating CD103^{int}CD11b$^+$DCs were also characterized by the intermediate expression of CD103, IRF8, and XCR1 (Figure S4H). These data show that hetIL-15 administration increased the number of the tumor-infiltrating CD103^{int}CD11b$^+$DCs in two different mouse models, indicating that this was a general hetIL-15-induced effect, independent of the mouse genetic background.

CD103^{int}CD11b$^+$DCs displayed a transcriptional signature similar to moDCs

To better characterize the properties of the different DC subsets localized in tumors, we performed RNA sequencing (RNA-seq) analysis on sorted tumor-infiltrating myeloid cell subsets. Principal-component analysis (PCA) of the different sorted populations (CD103$^+$cDC1, CD11b$^+$cDC2, CD103^{int}CD11b$^+$DC, and macrophages) based on their transcriptome profile revealed segregation of CD103^{int}CD11b$^+$DCs. These cells showed a transcriptomic profile close to CD11b$^+$cDC2s and mapped away from the macrophages in PCA space (Figure S5A). Comparison with immune cell transcriptome profiles reported by Brown et al.[50] confirmed that infiltrating CD103^{int}CD11b$^+$DCs showed low expression of the key macrophage genes *Fcgr1*, *Siglec1*, *Ly6c2*, *Cx3cr1*, and *Ly6c1*, whereas DC-expressed markers *CD24a*, *Xcr1*, *Itgae*, *Itgam*, *Itgax*, *Sirpa*, *Irf4*, *Cd207*, and *CD209a* (Figure S5B) were highly or intermediately expressed in tumor-infiltrating CD103^{int}CD11b$^+$DCs. This cell population had also increased *Rbpj* and *Batf3* gene expression but showed low expression of *CD8a* and *Flt3* (Figure S5B). To exclude the possibility of Flt3 dependence of tumor-infiltrating CD103^{int}CD11b$^+$DCs, we treated EO771 tumor-bearing mice with quizartinib (AC220), a Flt3-specific inhibitor, in combination with hetIL-15 treatment. Flow cytometric analysis of the tumor-infiltrating CD103^{int}CD11b$^+$DCs revealed that AC220 administration did not alter the number of the intratumoral CD103^{int}CD11b$^+$DC population (Figure S5C), verifying that CD103^{int}CD11b$^+$DC infiltration was not critically dependent on Flt3.

Furthermore, we generated a heatmap of the antigen-presentation pathway, using reference genes from Kaczanowska et al.,[51] which revealed that many genes implicated in antigen processing and presentation (*Wdfy4*, *Ciita*, *Naaa*, *Batf3*, *H2-DMa*, *H2-Aa*, *Cd74*, *H2-Ab1*, and *H2-Eb1*)[51–53] were upregulated in CD103^{int}CD11b$^+$DCs compared with other DC subsets or macrophages (Figure S5D). The high expression of genes

Figure 3. A distinct CD103^{int}CD11b$^+$DC population is detected in the hetIL-15-treated tumors

(A) Heatmap representing the estimated immune cell composition of tumors upon hetIL-15 treatment. Cell scores were calculated for different immune cell subsets as described in STAR Methods "method details" section.

(B) Gating and staining strategy used to identify distinct DC populations in the EO771 tumors. The CD103$^+$cDC1 (red), CD11b$^+$cDC2 (blue), and the CD103^{int}CD11b$^+$DC (green) populations are indicated in the contour plots.

(C–E) Flow cytometric analysis of intratumoral CD103$^+$cDC1 (C), CD11b$^+$cDC2 (D), and CD103^{int}CD11b$^+$DC (E) populations in controls and hetIL-15-treated mice. Data in graphs are given as absolute numbers of cells per gram of tissue and represented as mean ± SEM. Statistical significance was calculated by Mann-Whitney U test.

(F) Pearson correlation analysis between tumor volume (mm^3) and number of tumor-infiltrating DCs per gram of tissue. Data shown in (C)–(F) are pooled from three different experiments with n = 5–9 mice per group. The analysis wa conducted 48 h post-third hetIL-15 injection.

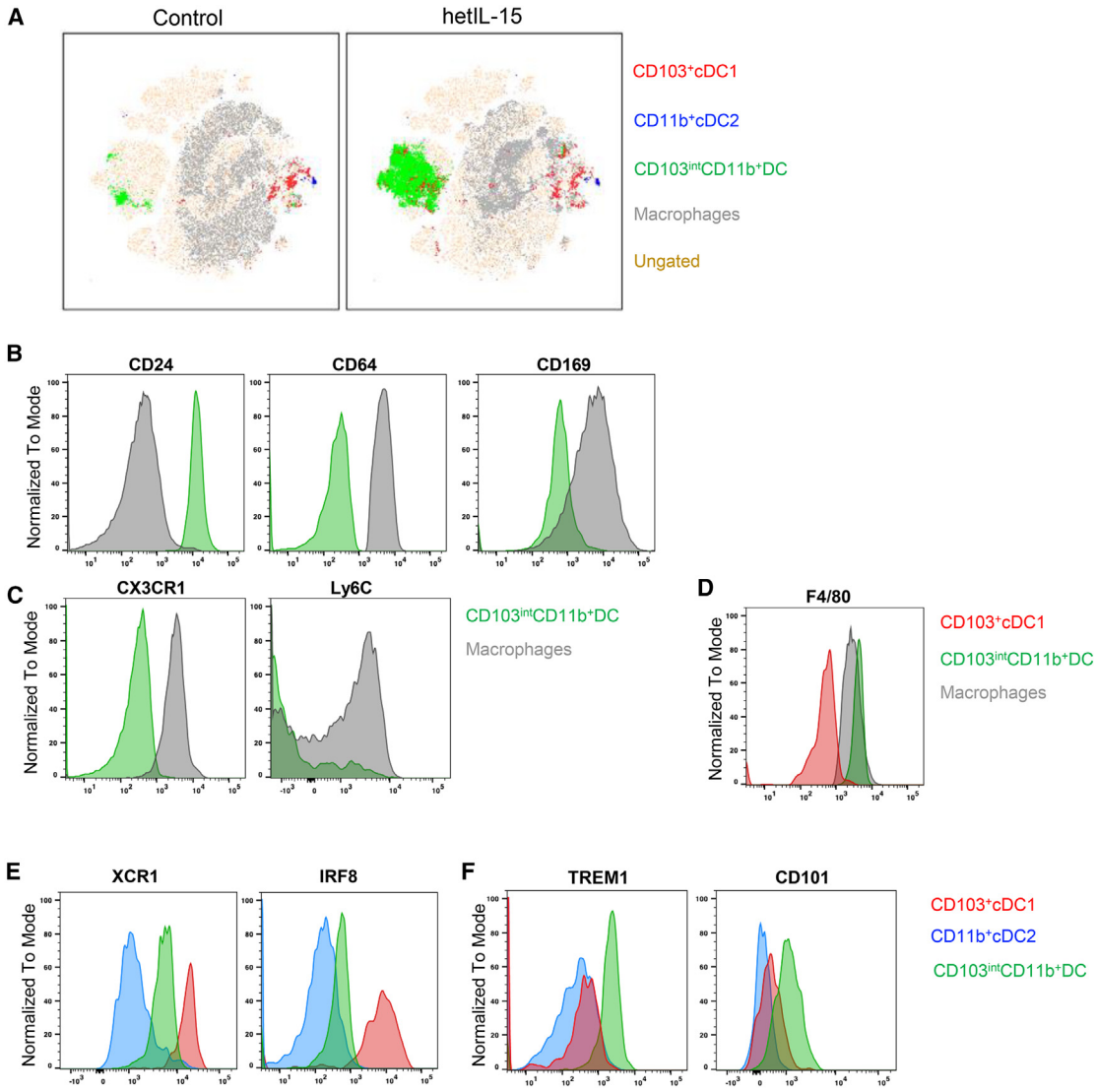

Figure 4. Phenotypic analysis of the novel tumor-infiltrating DC population

(A) t-SNE analysis of CD103$^+$cDC1, CD11b$^+$cDC2, CD103^{int}CD11b$^+$DC populations and macrophages based on multi-color flow cytometry generated from 11 concatenated samples; five samples from the control group and six samples from the hetIL-15-treated group.

(B–F) Histogram plots show the expression levels of CD24, CD64, CD169, CXC3R1, Ly6C (B and C); F4/80 (D); XCR1, IRF8 (E); and TREM1 and CD101 (F) on CD103$^+$cDC1 (red), CD11b$^+$cDC2 (blue), CD103^{int}CD11b$^+$DC (green) populations and macrophages (gray). Data are from three (CD24, CD64, F4/80, XCR1, IRF8) or two (CD169, CXCR3, Ly6C, TREM1, CD101) independent replicate experiments. The analysis was conducted 48 h post-third hetIL-15 injection.

involved in the antigen-presenting process as well as the correlation between the abundance of CD103^{int}CD11b$^+$DCs in hetIL-15-treated tumors and tumor growth control (Figure 3F) led to investigation of whether these cells contributed to the activation of CD8$^+$ T cells within the tumor. *Ex vivo* co-culture of isolated splenic CD8$^+$ T cells from naive mice with sorted DC populations (CD103$^+$cDC1, CD11b$^+$cDC2, or CD103^{int}CD11b$^+$DC) from hetIL-15-treated tumors led to induction of IFN-γ production in CD8$^+$ T cells from naive mice (Figure S5E). Therefore, CD103^{int}CD11b$^+$DCs were able to trigger *ex vivo* IFN-γ production similar to other APCs (CD103$^+$cDC1 and CD11b$^+$cDC2). Overall, these results showed that tumor-infiltrating CD103^{int} CD11b$^+$DCs have a unique transcriptomic profile, which differed from macrophages. Their signature involved genes encoding DC markers and contributing to DC functions, including genes involved in antigen presentation.

To further characterize the tumor-infiltrating CD103^{int} CD11b$^+$DCs, we performed single-cell RNA-seq (scRNA-seq) analysis on sorted CD11c$^+$ cells obtained from tumors of hetIL-15-treated or control EO771 tumor-bearing mice. A total of 10,195 single-cell transcriptomes were generated after pre-processing. Unsupervised clustering was performed using Seurat v3.1.5[54] and the Louvain method.[55] Clusters were serially annotated with SingleR using reference data generated from Brown

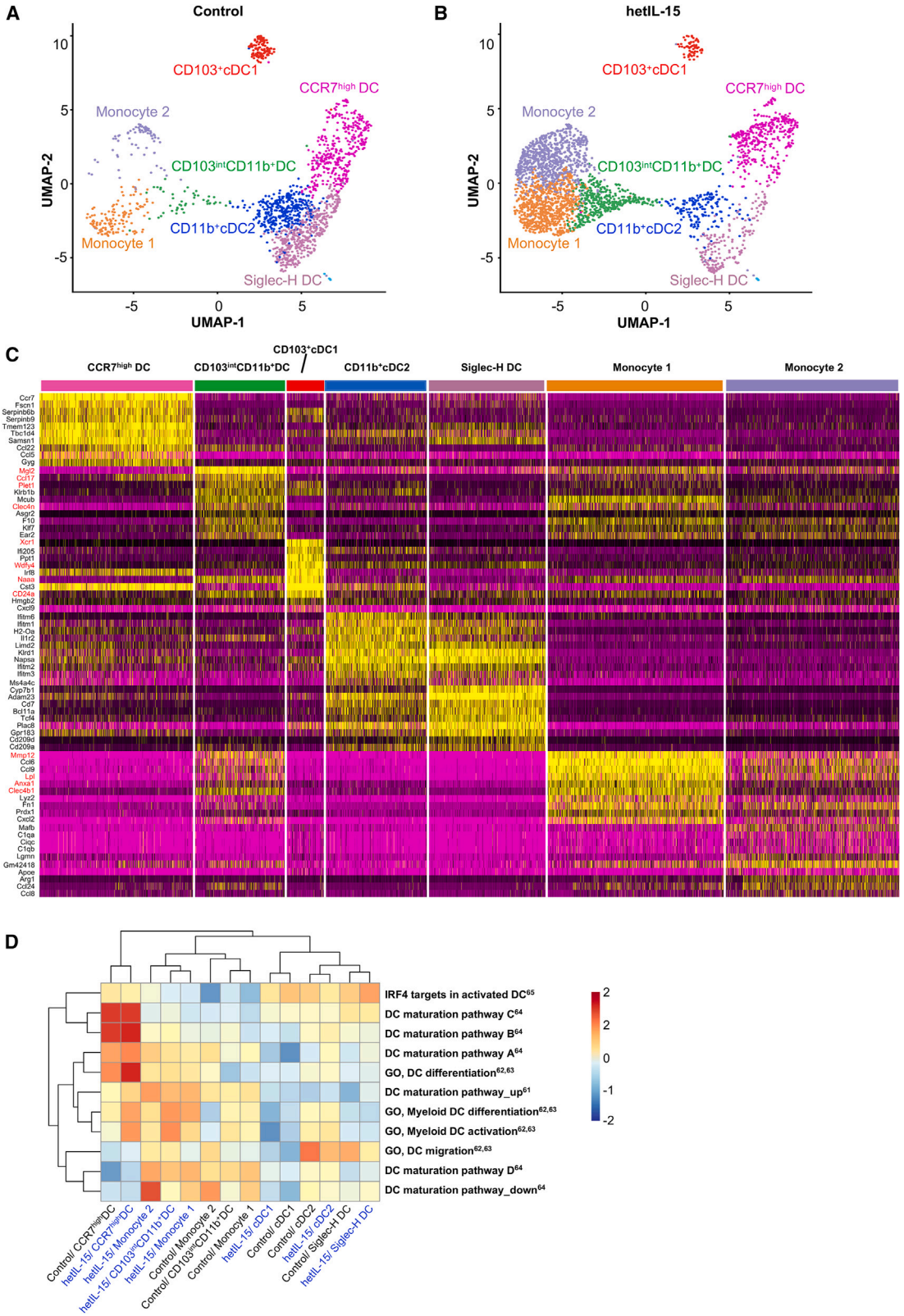

(legend on next page)

et al.[50] and RNA-seq matrices from our sorted DC populations. After removal of cell-cycle signals, scRNA-seq of the CD11c^{+}CD64^{neg} cells identified seven distinct clusters visualized using UMAP (Figures 5A and 5B). We established the cell identity of each cluster through the analysis of canonical DC gene expression similarity with reference genes from Brown et al.[50] The CD103^{int}CD11b^{+}DC population in hetIL-15-treated tumors was enriched in the sample density UMAP plot (Figure 5B, green). Cellular indexing of transcriptome and epitopes sequencing (CITE-seq) confirmed the high gene and protein expression of CD24 in CD103^{+}cDC1s and CD103^{int}CD11b^{+} DCs (Figure S6A, yellow at bottom panel). The CD103^{int}CD11b^{+} DC population expressed a unique gene signature. Shared gene expression among individual clusters revealed that CD103^{int}CD11b^{+}DCs possessed a gene profile with similarities to monocytes (monocyte 1 cluster, Figure 5C), with several highly expressed moDC/DC markers (*Mgl2*, *Ccl17*, *Plet1*, *Clec4n* [Dectin2], *CD24a*, *mmp12*, *clec4b1* [DCAR], and *Anxa1* [Annexin1]),[46,56–60] suggesting a possible monocytic origin for this DC subset. CD103^{int}CD11b^{+}DCs expressed the highest levels of *Mgl2* and *Ccl17* among the different DC subtypes. *Plet1*, a specific marker of cDC2s in the gastrointestinal tract, and *Mmp12*, which is expressed in both resting and activated human moDCs,[59] were also highly expressed in the CD103^{int}CD11b^{+}DC cluster. In addition, CD103^{int}CD11b^{+}DCs were characterized by high levels of *Clec4b1*, a protein that is selectively expressed in mouse CD11b^{+}CD11c^{int}MHCII^{+} monocyte-derived cells,[57] and *Lpl*, as in the human moDCs.[61] The Increased expression of genes related to antigen-processing machinery of DCs, such as *Naaa*, *Wdfy*4, and *Annexin1*,[52,53,56] was also verified in the CD103^{int}CD11b^{+}DCs. Bubble plot of canonical DC and selected macrophage/monocyte markers[50] verified the absence of macrophage markers (*Cx3cr1*, *Ly6c1*, *Siglec1*), the decreased expression of *Flt3*, and the increased expression of moDC/DC markers (*CD24a*, *Itgam*, *Itgax*, *Sirpa*, and *Lamp2*) in CD103^{int}CD11b^{+}DCs (Figure S6B). Interestingly, single-sample gene set enrichment analysis (ssGSEA) revealed enrichment of pathways involved in DC migration and maturation, as well as myeloid DC differentiation and activation,[60–65] in the tumor-infiltrating CD103^{int}CD11b^{+}DC cluster after hetIL-15 treatment (Figure 5D). Furthermore, transcriptomic cytokine profiling of cDCs and CD103^{int}CD11b^{+}DCs revealed that CD103^{int}CD11b^{+}DCs expressed higher levels of inflammatory chemokines *Ccl6*, *Ccl9*, *Cxcl2*, *Ccl17*, *Ccl2*, *Ccl4*, *Ccl22*, and *Ccl24* compared with other DC subtypes (Figure S6C). Overall, our RNA-seq data demonstrated that CD103^{int} CD11b^{+}DCs formed a distinct cluster with a transcriptional profile with similarities to moDCs and may have a functional, intratumoral role due to the expression of genes associated with antigen presentation.

Our scRNA-seq results demonstrated that CD103^{int}CD11b^{+} DCs had the highest expression levels of *Mgl2* and *Ccl17* among the different DC subtypes and monocytes and also expressed *CD24a*. We reasoned that co-expression of these highly express markers can uniquely identify the group of CD103^{int}CD11b^{+}DCs. Therefore, we performed *in situ* RNA hybridization (RNAScope), using probes that target these three markers, in paraffin-embedded tumor tissues to further identify the presence and localization of this unique DC population. RNAScope analysis confirmed the presence of CD103^{int}CD11b^{+}DCs in the tumors of hetIL-15-treated mice. In contrast, CD103^{int}CD11b^{+}DCs could not be detected in the tumors from control mice (Figure 6) and in dLNs of hetIL-15-treated or untreated mice, shown by RNAScope (Figure S7A) and flow cytometric (Figure S7B) analyses. Furthermore, RNAScope analysis was performed in paraffin-embedded tumor from EO771 tumor-bearing NK cell-depleted C57BL/6 or *Rag-1* ko mice that had been treated with hetIL-15. *In situ* hybridization verified the decreased accumulation of CD103^{int}CD11b^{+}DCs in the absence of NK cells (Figure S8). Interestingly, although we observed many CD103^{int}CD11b^{+}DCs in the tumors from the hetIL-15-treated *Rag-1* ko mice, those cells were found only in the peripheral regions of the tumor (Figure S9).

hetIL-15 locoregional administration resulted in a long-lasting specific anti-tumor immunity

We also examined the development of anti-tumor memory T cells upon locoregional hetIL-15 administration. Mice that had previously eradicated EO771 tumors were rechallenged with the same tumor cell line at 68 and 158 days after the last hetIL-15 dose (Figure 7A). Age-matched control mice developed EO771 tumors as expected, whereas tumors failed to be established in mice with a previous history of tumor eradication after hetIL-15 therapy, suggesting development of protective anti-tumor immunity (Figure 7B). To verify the specificity of the anti-tumor immune response, mice were also challenged using the syngeneic pancreatic Kras-p53-Cre (KPC) tumor cells (challenge #2, Figure 7A). KPC tumors developed at the same rate in both groups (Figure 7C), supporting the conclusion that hetIL-15-treated mice were able to develop and maintain specific immunity against EO771 tumor.

Next, we performed adoptive cell transfer of purified CD8^{+} T cells from hetIL-15-treated mice that had previously eradicated EO771 tumors and successfully rejected EO771 tumors upon subsequent re-challenge (Figure 7D). Recipients were treated with hetIL-15 every 2 days to support the adoptively transferred CD8^{+} T cells. Transfer of the CD8^{+} T cells into lymphodepleted EO771 tumor-bearing mice reduced tumor growth (Figure 7E, left panel) and increased the survival of

Figure 5. scRNA-seq analysis revealed that hetIL-15-induced CD103^{int}CD11b^{+}DCs share transcriptional similarities with moDCs and cDCs

Isolated tumor-infiltrating CD11c^{+} populations from control and hetIL15-treated EO771 tumor-bearing mice were processed into single-cell suspension.

(A and B) UMAP plot of scRNA-seq analysis of CD11c^{+} tumor-infiltrating cells serially annotated with SingleR[50] from control (A) or hetIL15-treated (B) sample.

(C) Heatmap reporting scaled, imputed expression of the top 10 differentially expressed genes for each cluster across all cells, identified in (A). Genes of interest are shown on the left in red.

(D) Heatmap showing DC different pathways enriched in the integrated tumor-infiltrating CD11c^{+} clusters by GSEA analysis, colored by *Z* score transformed mean GSEA scores. The analysis was conducted 48 h post-third hetIL-15 injection.

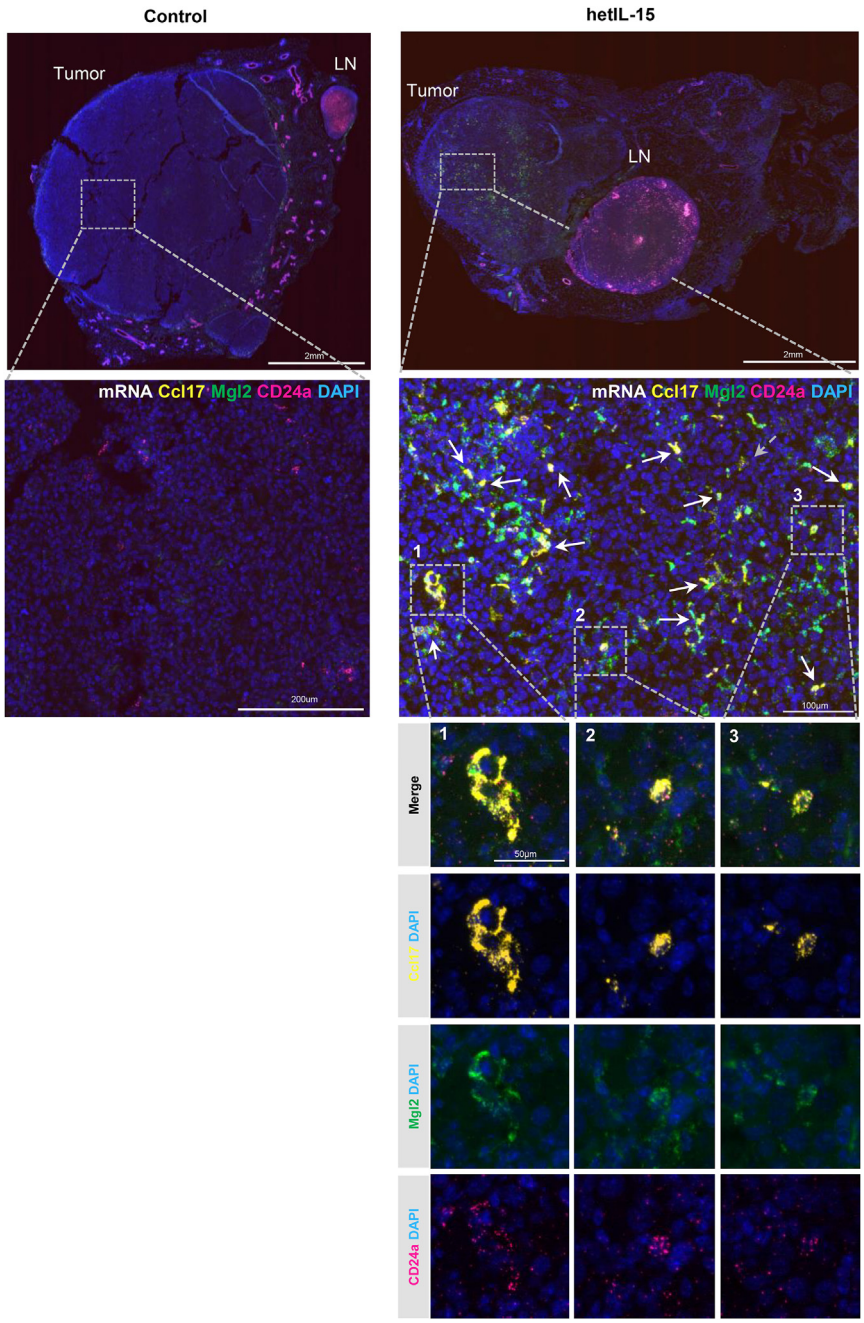

Figure 6. Triple RNA *in situ* hybridization (RNAScope) of EO771 cancer samples verified the presence of the CD103^{int}CD11b^{+} DCs in the tumors of the hetIL-15-treated mice

Triple RNA *in situ* hybridization of EO771 cancer samples verified the presence of the CD103^{int}CD11b^{+}DCs in the tumors of hetIL-15-treated mice, 48 h after the third hetIL-15 injection. Low-magnification images (2 mm, upper panel) and 20× images (200 μm, control group and 100 μm, hetIL-15 group, middle panel) showing the expression of *Ccl17* (yellow), *Mgl2* (green), and *CD24a* (pink) mRNA in paraffin-embedded tissue. High-magnification (40×, 50 μm, bottom) of area (1), (2), and (3) individual images showing CD103^{int}CD11b^{+}DCs expressing *Mgl2*, *Ccl17*, and *CD24a*. Nuclear staining using DAPI (blue). White arrows indicate the CD103^{int}CD11b^{+}DCs. Representative images from one experiment with n = 5 mice per group.

the recipient mice (Figure 7E, right panel) compared with mice receiving CD8^{+} T cells from mice never exposed to EO771 tumor cells. We also monitored the development of lung metastasis in mice that underwent adoptive cell transfer of CD8^{+} T cells. The number of lung tumor foci in mice that received CD8^{+} T cells from donors previously cured from EO771 was significantly reduced (Figure 7F), suggesting that hetIL-15-induced memory CD8^{+} T cells could reduce or control metastatic disease in the lungs. Overall, our findings indicated that monotherapy using locoregional hetIL-15 administration caused the development of specific long-lasting anti-tumor immunity, which resulted in complete tumor eradication and protection from subsequent exposure.

DISCUSSION

The present study provides evidence that hetIL-15 administration, in proximity to the tumor, is a therapeutic approach with strong activity against TNBC that exerts both local and systemic effects. These effects include cures of the tumor-bearing mice (~40%), prolonged survival, and induction of immunological memory against breast cancer cells. Reduction or complete elimination of metastatic disease was also observed. This result on metastatic reduction is also supported by our recently reported findings in the 4T1 mouse TNBC model.[66] Another important conclusion of this work is that hetIL-15 re-shaped the tumor microenvironment by promoting the intratumoral accumulation of cytotoxic lymphocytes, cDC1s, and a distinct DC population, defined as CD103^{int}CD11b^{+}DC. This distinct DC population has phenotypic and transcriptional similarities with cDCs and moDCs and correlates with tumor regression.

There is an increased interest on exploring local delivery of immune modulators for the treatment of solid tumors. Several studies reviewed by Marabelle et al.[67] have shown that intratumoral administration of immune-stimulating drugs allows for higher concentrations in the tumor microenvironment than systemic deliveries, resulting in improved therapeutic effects and lower toxicities. As a result, the number of trials investigating local administration of cancer therapies has experienced rapid

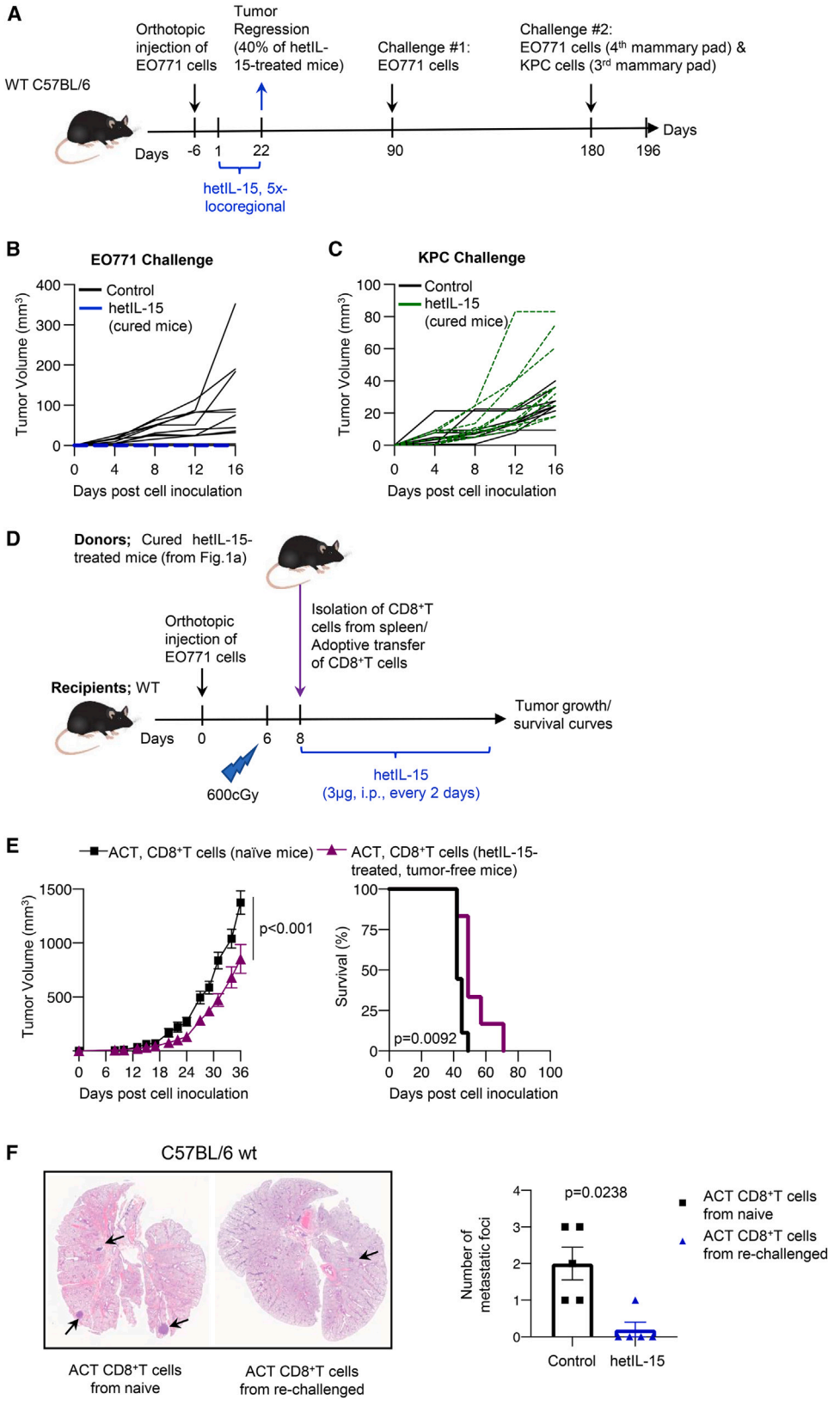

(legend on next page)

growth.[68] Different forms of IL-15 have been investigated as cancer immunotherapeutics in several mouse cancer models[28–32,69] and they are currently being tested in several clinical trials.[33–39] The first-in-human trial with hetIL-15 delivered systemically by subcutaneous injection in patients with metastatic or unresectable cancer showed disease stabilization in three of the 14 participants as the best observed clinical response,[33] but hetIL-15 has not yet been evaluated in human breast cancer.

In our mouse orthotopic breast model, hetIL-15 locoregional administration increased therapeutic effects by resulting in complete tumor regression and elimination or decrease in metastasis. hetIL-15 was given using Matrigel as vehicle, which might contribute to the efficacy by retaining the cytokine close to the tumor area. hetIL-15 monotherapy stimulated $CD8^+$ T and NK cells trafficking into the tumors and promoted their proliferation and cytotoxicity. These data agree with preclinical and clinical studies where the anti-tumor responses induced by IL-15 were linked to expansion and activation of NK and $CD8^+$ T cells.[28,34,70,71] Importantly, our depletion experiments suggest that the effects of hetIL-15 treatment in controlling tumor growth and metastasis in a TNBC model were mediated through both T and NK cells. Significant tumor growth delay was observed after locoregional injection of hetIL-15 in *Rag-1* ko and NK cell-depleted C57BL/6 mice. However, complete tumor regression was not achieved in *Rag-1* ko mice, suggesting that adaptive immunity is required for the curative effect of hetIL-15. We also demonstrated that EO771-tumor elimination in mice after hetIL-15 monotherapy provided T cell-dependent protection from subsequent rechallenge with EO771 tumor. These data support the conclusion that hetIL-15 elicits long-term T cell memory against tumor cells. The preserved T cell responses were specific for the EO771 tumors because those animals failed to control challenge with an unrelated syngeneic pancreatic tumor line.

Effects of IL-15 on DC phenotypic characteristics and functions have been previously reported.[72–77] Here, we show that locoregional administration of hetIL-15 increases tumor-infiltrating $CD103^+$cDC1s in EO771 orthotopic breast cancer model and this accumulation is inversely correlated with tumor size. These results agree with our previous report where systemic hetIL-15 delivery increased the intratumoral $CD103^+$cDC1s of MC-38 and TC-1 tumors.[28] Importantly, we identified a discrete $CD103^{int}CD11b^+$DC subset that greatly increased in tumors upon hetIL-15 treatment, while it is present in very low numbers in the control group. This population also inversely correlated with EO771 tumor size. Its intratumoral accumulation and localization within the tumor was dependent on the NK, T, or B cells. In the absence of T and B cells, $CD103^{int}CD11b^+$DCs accumulated in the periphery of the tumor, whereas NK cell depletion resulted in lower numbers of $CD103^{int}CD11b^+$DCs. It has been reported that $CD103^+$cDC1s accumulation in mouse tumors often depends on NK cells producing the chemokines CCL5 and XCL1.[44] The induced DC population expresses XCR1 and can presumably be attracted to XCL1 expressing cells. However, the relative contributions of the mechanisms by which NK and T cells contribute to the tumor infiltration and function of $CD103^{int}CD11b^+$DCs remains to be verified.

The $CD103^{int}CD11b^+$DC population was also identified in the 4T1 mouse model of TNBC and found elevated in tumors upon hetIL-15 treatment, suggesting a general effect of hetIL-15 on expanding this DC population in tumors developing in different mouse strains. Despite the accumulation of $CD103^{int}$ $CD11b^+$DCs especially in the treated tumors, those cells were not present in the dLNs. None of the DC subpopulations identified in dLNs display the same profile with the $CD103^{int}$ $CD11b^+$DCs suggesting that either the $CD103^{int}CD11b^+$DCs migrate to the dLNs in small numbers and transiently, or that their phenotypic profile changes upon migration and maturation[11,78–80] and therefore cannot be identified using the same markers as in the tumor.

Combination of scRNA-seq, bulk RNA-seq, and flow cytometric analysis suggests a possible monocytic origin for $CD103^{int}CD11b^+$DCs. Shared gene expression among individual clusters revealed that $CD103^{int}CD11b^+$DCs possess a gene profile with similarities to monocytes, with several highly expressed moDC/DC markers but also several differences from macrophages. They lack many key macrophage markers *Fcgr1* (CD64), CD169, *Cx3cr1* (CX3CR1), *Ly6c1* (L6c1), and *Siglec1* but they express F4/80. This common macrophage marker has, however, been found expressed by another DC subset, the monocyte-derived migratory APCs, $F4/80^{high}$APCs.[80] Our

Figure 7. hetIL-15 locoregional administration provided long-lasting specific anti-tumor immunity

(A) Timeline of repetitive tumor challenge. On day −6, C57BL/6 mice were inoculated with EO771 cells (3×10^5, orthotopically in the fourth mammary pad). Starting 7 days later, mice were treated with five hetIL-15 injections (5 μg/dose/mouse) every 4 days. On day 90, long-term surviving tumor-free mice were rechallenged (challenge #1) by injection of EO771 cells (5×10^4, orthotopically in the fourth mammary pad). No tumor growth was detected and on day 180, the mice were rechallenged (challenge #2) by injection of EO771 cells (5×10^4, orthotopically in the fourth mammary pad) and by injection of KPC cells (5×10^4, orthotopically in the third mammary pad). The endpoint time of this experiment was day 196.

(B and C) Growth of individual EO771 (B) and KPC tumors (C) were monitored from day 180 (challenge #2) until the endpoint. Data are pooled from two experiments with five mice per group.

(D) Schematic representation of adoptive transfer of tumor immunity. Recipient mice were challenged with EO771 cells (5×10^4, orthotopically in the fourth mammary pad) on day 0; 6 days later, the mice were irradiated with 600 cGy. Eight days after tumor challenge, $CD8^+$ T cells from spleen of naive or rechallenged mice from Figure 7A were isolated and injected into the EO771 tumor-bearing mice. Recipient mice were then boosted with hetIL-15 intraperitoneal (i.p.) injections (5 μg/dose/mouse) every 2 days until the endpoint.

(E) EO771 tumor size (left) and survival curve (right) following adoptive transfer. Data shown in (E, left) are pooled from two experiments with five to eight mice per group and represented as mean ± SEM. Data in (E, right) are from one of two similar experiments. Statistical significance was calculated by mixed-effects analysis (E, left) and for survival (E, right) by log rank (Mantel-Cox) test.

(F) H&E staining of representative lung metastases and the corresponding actual counts per slide of lung metastatic foci in C57BL/6 recipient mice that underwent adoptive cell transfer of $CD8^+$ T cells from Figure 7D. Data shown are from one experiment (n = 5 mice per group) and represented as mean ± SEM. Statistical significance was calculated by Mann-Whitney U test.

CD103^{int}CD11b^{+}DCs have similarities to the F4/80^{high}APCs, but they do not express CD64 and CD169. Further characterization of CD103^{int}CD11b^{+}DCs showed that they have intermediate expression of XCR1 and IRF8. These markers distinguish CD103^{int}CD11b^{+}DCs from both the cDC1 and cDC2 populations. XCR1 expression is strongly associated with the ability of cDC1s to interact with CD8^{+} T cells,[81] whereas IRF8 strongly correlated with their cross-presenting phenotype.[82] In addition, CD103^{int}CD11b^{+} DCs have increased *Rbpj* and *Batf3* gene expression. It has been shown that the transcription factor RBP-J-mediated signaling is essential for DCs to evoke efficient anti-tumor immune responses in mice,[83] whereas Batf3-lineage CD103^{+} DCs are necessary for recruitment of effector CD8^{+} T cells within the tumor.[84] Furthermore, CD103^{int}CD11b^{+} DCs demonstrated decreased *Flt3* gene expression, which is absent from the *in vitro* differentiated moDCs,[85] while flow cytometric analysis verified that tumor accumulation of CD103^{int}CD11b^{+}DCs is Flt3 independent. The tumor-infiltrating CD103^{int}CD11b^{+}DCs have a distinct expression pattern of CD64, CD24, F4/80, CD103, and XCR1 genes that distinguishes them from most DC populations that have been previously reported in the literature, including the inflammatory cDC2s,[86] the tumor moDC3s,[87] the PDAC-associated CD11c^{+}DCs,[88] or the mouse dermal moDCs.[17] The expression pattern of the tumor-infiltrating CD103^{int}CD11b^{+}DCs shows similarities with the intestinal CD103^{+}CD11b^{+}DCs and some types of moDCs. CD103^{+}CD11b^{+}DCs in the intestinal lamina propria express high levels of *Gp2*, *Cd101*, and *Trem1*.[48,49] We examined whether these markers were expressed in the hetIL-15-induced CD103^{int}CD11b^{+}DCs. Although we could not detect any surface expression of GP2, expression of TREM1 and CD101 was higher compared with cDC1 and cDC2 subtypes. Furthermore, the CD103^{int}CD11b^{+}DCs express low levels of the chemokine receptor CX3CR1, which was also observed in intestinal CD103^{+}CD11b^{+}DCs,[48] supporting the notion that these cells are not tissue-resident macrophages.

Single-cell transcriptomic analysis also showed that CD103^{int}CD11b^{+}DCs induced by hetIL-15 share similarities in transcribed genes with the moDCs and more specifically with (1) the CD64^{-}MHC^{+}CD11c^{+}Ly6C^{lo}CX3CR1^{int}moDCs, which display migratory and antigen-presenting features,[89–91] and (2) with the Ly6C^{lo}CD209a^{+}moDCs, which are powerful migratory antigen-capturing cells and APCs.[18] Several reports have provided evidence that the immune system uses monocytes as DC precursors for efficient antigenic presentation in the periphery during inflammation[92–94] and suggesting that moDCs are important players in the development of an adaptive immune response.[46] Many genes associated with antigen processing and presentation (*Wdfy4*, *Ciita*, *Naaa*, *Batf3*, *H2-DMa*, *H2-Aa*, *Cd74*, *H2-Ab1*, and *H2-Eb1*)[51–53] were highly expressed in hetIL-15-induced tumor-infiltrating CD103^{int}CD11b^{+}DCs, suggesting the antigen-presenting properties of those cells. Importantly, transcriptomic cytokine profiling revealed high expression of *Cxcl2*, *Ccl17*, and *Ccl22*, suggesting that CD103^{int}CD11b^{+}DCs may be activated or mature moDCs/cDCs[78,95,96] and are involved in the recruitment of activated and memory T cells, as well as B lymphocytes.[16,78,97–100] The gene set enrichment analysis (GSEA) of our CD103^{int}CD11b^{+}DCs scRNA-seq data strengthen this hypothesis since it revealed the upregulation of many cellular processes involved in the maturation and activation of DCs. Furthermore, CD103^{int}CD11b^{+}DCs expressed the highest levels of *Mgl2* and *Ccl17* among the different DC subtypes. CCL17^{+} DCs, distributed in most lymphoid and non-lymphoid tissues, represent a mature subset of DCs with high capacity of inducing T cell-mediated immune response.[78] The high expression of *Mgl2* in CD103^{int}CD11b^{+} DCs raises the question of whether Mgl2^{+}dermal DCs, previously reported in the skin and the draining popliteal LN,[14] are akin to CD103^{int}CD11b^{+}DCs. Mgl2^{+}DCs in the lamina propria have been identified as the APCs responsible for driving tissue-resident memory CD8^{+} T cell-mediated protection after HSV-2 infection,[101] while it was reported that Mgl2 is preferentially expressed on cDCs and involved in the efficient uptake and presentation of antigens with GalNac residues.[102] Moreover, *CLEC10A*, the human homolog to the *Mgl2*, is a key marker for the CD1c^{+}DCs.[103] When properly activated, human CD1c (BDCA-1)$^{+}$ myeloid-derived DCs (myDCs) secrete high levels of interleukin-12 (IL-12) and potently prime cytotoxic T lymphocyte (CTL) responses.[104] The therapeutic potential of cellular vaccines that contain antigen-loaded CD1c (BDCA-1)$^{+}$myDCs has already been under investigation in early clinical trials in patients with metastatic melanoma or prostate cancer indicating objective tumor responses and immunogenicity.[105–107] These properties of the human CD1c^{+}DCs further suggest possible involvement of CD103^{int}CD11b^{+}DCs in antigen presentation and immune response and underscore a role of hetIL-15 in these processes. The finding that the CD103^{int}CD11b^{+}DCs are not present in the dLNs and are only found in the periphery of the tumor in the absence of CD8^{+} T cells suggests that the interaction between CD8^{+} T cells and the CD103^{int}CD11b^{+}DCs may be occurring specifically within the tumor microenvironment. Alternatively, the phenotype of DC populations may change depending on the environment and trafficking; therefore, further studies are necessary to determine their functional role and their cross-presenting capabilities.

In conclusion, locoregional therapy with hetIL-15 is effective and holds promise as a future therapeutic option for TNBC. hetIL-15 coordinates an effective local and systemic immune response against TNBC tumors in different mouse models, promoting tumor killing by CD8^{+} T and NK cells and increasing tumor infiltration of cDC1s and of a unique CD103^{int}CD11b^{+} DC subpopulation most closely related to moDCs. These cells may represent an additional mechanism of tumor recognition and anti-tumoral immune response under circumstances where professional cross-presenting cDC1s have become limited or dysregulated, such as in inflammatory tumor tissue.[80,108,109] This report demonstrates that hetIL-15 administration enhanced the intratumoral interaction between DCs and lymphocytes, leading to the generation of a long-lasting specific and protective anti-tumoral immune response.

Limitations of the study

The mechanism of function of DC subpopulations and their relative contribution to tumor eradication is not understood completely and requires additional experiments. Specific ko studies depleting selective cell subpopulation may advance our

understanding, but it is not clear which genes are both unique and essential for function of these DC subpopulations. Additional work is required to fully understand the definitive origin and functional differences between DC populations and whether the specific immunity developing after hetIL-15 tumor eradication depends on a specific DC subset. The human counterparts of these DCs have not been identified and remain to be elucidated.

STAR★METHODS

Detailed methods are provided in the online version of this paper and include the following:

- KEY RESOURCES TABLE
- RESOURCE AVAILABILITY
  - Lead contact
  - Materials availability
  - Data and code availability
- EXPERIMENTAL MODEL AND SUBJECT DETAILS
  - Mouse models and animal ethics statement
  - Immunotherapy of EO771 or 4T1 tumor-bearing mice
  - NK cell depletion *in vivo*
  - Adoptive cell transfer
  - Rechallenge experiments
- METHOD DETAILS
  - Histology and immunohistochemistry staining
  - Splenic $CD8a^+$T cells isolation
  - Tumor-infiltrating $CD11c^+$ cell isolation
  - Flow cytometry
  - Gene expression analysis by nCounter PanCancer Immune Profiling Panel
  - Bulk RNA sequencing
  - CITE- and single-cell RNA-sequencing
  - Multiplex RNA *in situ* hybridization staining
  - Direct co-culture of DCs with $CD8^+$ T cells
- QUANTIFICATION AND STATISTICAL ANALYSIS

SUPPLEMENTAL INFORMATION

Supplemental information can be found online at https://doi.org/10.1016/j.celrep.2023.112501.

ACKNOWLEDGMENTS

We thank A. Valentin for support and discussions; K. Klarmann, CCR-Frederick Flow Cytometry Core Laboratory; T. Bao, J. Shetty, and M. Mehta, sequencing facility; A. Warner, Molecular Histopathology Laboratory; X. Wu and N. Bubunenko, Genomics Laboratory; A. Kane, Scientific Publications, Graphics, and Media, Frederick National Laboratory for Cancer Research for technical assistance; members of Pavlakis and Felber labs for discussions and support; and T. Jones for editorial assistance. This work was funded by the Intramural Research Program of the National Cancer Institute, National Institutes of Health (NCI/NIH) (B.K.F. and G.N.P.). This work was also supported by an NCI Collaborative Research Agreement (CRADA#02199) with Novartis. This project has been funded in part with federal funds from the National Cancer Institute, National Institutes of Health, under contract no. HHSN261201500003I. The content of this publication does not necessarily reflect the views or policies of the Department of Health and Human Services, nor does mention of trade names, commercial products, or organizations imply endorsement by the US Government. This contract number represents work performed within the scope of work of the non-severable IDIQ contract.

AUTHOR CONTRIBUTIONS

Conceptualization, D.S., S.K., and G.N.P.; performed experiments, D.S., S.K., V.S., and B.A.N.; analyzed data, D.S., S.K., and V.S.; analyzed transcriptomic data, M.A. and K.C.G.; investigation, D.S., S.K., and V.S.; visualization, D.S., S.K., and G.N.P.; funding acquisition, B.K.F. and G.N.P.; supervision, G.N.P.; writing – original draft, D.S. and S.K.; writing – review & editing, D.S., S.K., V.S., C.B., B.K.F., and G.N.P.; review final manuscript, D.S., S.K., V.S., M.A., K.C.G., B.A.N., C.B., B.K.F., and G.N.P.

DECLARATION OF INTERESTS

B.K.F., C.B., and G.N.P. are inventors on US Government-owned patents related to hetIL-15.

INCLUSION AND DIVERSITY

We support inclusive, diverse, and equitable conduct of research.

Received: July 8, 2022
Revised: March 5, 2023
Accepted: April 27, 2023
Published: May 12, 2023

REFERENCES

1. Dent, R., Trudeau, M., Pritchard, K.I., Hanna, W.M., Kahn, H.K., Sawka, C.A., Lickley, L.A., Rawlinson, E., Sun, P., and Narod, S.A. (2007). Triple-negative breast cancer: clinical features and patterns of recurrence. Clin. Cancer Res. *13*, 4429–4434. https://doi.org/10.1158/1078-0432.CCR-06-3045.
2. Siegel, R.L., Miller, K.D., and Jemal, A. (2018). Cancer statistics. CA A Cancer J. Clin. *68*, 7–30. https://doi.org/10.3322/caac.21442.
3. Torres, E.T.R., and Emens, L.A. (2022). Emerging combination immunotherapy strategies for breast cancer: dual immune checkpoint modulation, antibody-drug conjugates and bispecific antibodies. Breast Cancer Res. Treat. *191*, 291–302. https://doi.org/10.1007/s10549-021-06423-0.
4. Loi, S., Drubay, D., Adams, S., Pruneri, G., Francis, P.A., Lacroix-Triki, M., Joensuu, H., Dieci, M.V., Badve, S., Demaria, S., et al. (2019). Tumor-infiltrating lymphocytes and prognosis: a pooled individual patient analysis of early-stage triple-negative breast cancers. J. Clin. Oncol. *37*, 559–569. https://doi.org/10.1200/JCO.18.01010.
5. Criscitiello, C., Esposito, A., Trapani, D., and Curigliano, G. (2016). Prognostic and predictive value of tumor infiltrating lymphocytes in early breast cancer. Cancer Treat Rev. *50*, 205–207. https://doi.org/10.1016/j.ctrv.2016.09.019.
6. Zhang, S., Ma, X., Zhu, C., Liu, L., Wang, G., and Yuan, X. (2016). The role of myeloid-derived suppressor cells in patients with solid tumors: a meta-analysis. PLoS One *11*, e0164514. https://doi.org/10.1371/journal.pone.0164514.
7. Casbon, A.J., Reynaud, D., Park, C., Khuc, E., Gan, D.D., Schepers, K., Passegué, E., and Werb, Z. (2015). Invasive breast cancer reprograms early myeloid differentiation in the bone marrow to generate immunosuppressive neutrophils. Proc. Natl. Acad. Sci. USA *112*, E566–E575. https://doi.org/10.1073/pnas.1424927112.
8. Lee, H., Lee, H.J., Song, I.H., Bang, W.S., Heo, S.H., Gong, G., and Park, I.A. (2018). CD11c-Positive dendritic cells in triple-negative breast cancer. In Vivo *32*, 1561–1569. https://doi.org/10.21873/invivo.11415.
9. Bosteels, C., and Scott, C.L. (2020). Transcriptional regulation of DC fate specification. Mol. Immunol. *121*, 38–46. https://doi.org/10.1016/j.molimm.2020.02.021.
10. Cabeza-Cabrerizo, M., Cardoso, A., Minutti, C.M., Pereira da Costa, M., and Reis e Sousa, C. (2021). Dendritic cells revisited. Annu. Rev. Immunol. *39*, 131–166. https://doi.org/10.1146/annurev-immunol-061020-053707.

11. Guilliams, M., Dutertre, C.A., Scott, C.L., McGovern, N., Sichien, D., Chakarov, S., Van Gassen, S., Chen, J., Poidinger, M., De Prijck, S., et al. (2016). Unsupervised high-dimensional analysis aligns dendritic cells across tissues and species. Immunity *45*, 669–684. https://doi.org/10.1016/j.immuni.2016.08.015.

12. Murphy, T.L., Grajales-Reyes, G.E., Wu, X., Tussiwand, R., Briseño, C.G., Iwata, A., Kretzer, N.M., Durai, V., and Murphy, K.M. (2016). Transcriptional control of dendritic cell development. Annu. Rev. Immunol. *34*, 93–119. https://doi.org/10.1146/annurev-immunol-032713-120204.

13. Durai, V., and Murphy, K.M. (2016). Functions of murine dendritic cells. Immunity *45*, 719–736. https://doi.org/10.1016/j.immuni.2016.10.010.

14. Kumamoto, Y., Linehan, M., Weinstein, J.S., Laidlaw, B.J., Craft, J.E., and Iwasaki, A. (2013). CD301b(+) dermal dendritic cells drive T helper 2 cell-mediated immunity. Immunity *39*, 733–743. https://doi.org/10.1016/j.immuni.2013.08.029.

15. Williams, J.W., Tjota, M.Y., Clay, B.S., Vander Lugt, B., Bandukwala, H.S., Hrusch, C.L., Decker, D.C., Blaine, K.M., Fixsen, B.R., Singh, H., et al. (2013). Transcription factor IRF4 drives dendritic cells to promote Th2 differentiation. Nat. Commun. *4*, 2990. https://doi.org/10.1038/ncomms3990.

16. Plantinga, M., Guilliams, M., Vanheerswynghels, M., Deswarte, K., Branco-Madeira, F., Toussaint, W., Vanhoutte, L., Neyt, K., Killeen, N., Malissen, B., et al. (2013). Conventional and monocyte-derived CD11b(+) dendritic cells initiate and maintain T helper 2 cell-mediated immunity to house dust mite allergen. Immunity *38*, 322–335. https://doi.org/10.1016/j.immuni.2012.10.016.

17. Tamoutounour, S., Guilliams, M., Montanana Sanchis, F., Liu, H., Terhorst, D., Malosse, C., Pollet, E., Ardouin, L., Luche, H., Sanchez, C., et al. (2013). Origins and functional specialization of macrophages and of conventional and monocyte-derived dendritic cells in mouse skin. Immunity *39*, 925–938. https://doi.org/10.1016/j.immuni.2013.10.004.

18. Cheong, C., Matos, I., Choi, J.H., Dandamudi, D.B., Shrestha, E., Longhi, M.P., Jeffrey, K.L., Anthony, R.M., Kluger, C., Nchinda, G., et al. (2010). Microbial stimulation fully differentiates monocytes to DC-SIGN/CD209(+) dendritic cells for immune T cell areas. Cell *143*, 416–429. https://doi.org/10.1016/j.cell.2010.09.039.

19. Kool, M., Soullié, T., van Nimwegen, M., Willart, M.A.M., Muskens, F., Jung, S., Hoogsteden, H.C., Hammad, H., and Lambrecht, B.N. (2008). Alum adjuvant boosts adaptive immunity by inducing uric acid and activating inflammatory dendritic cells. J. Exp. Med. *205*, 869–882. https://doi.org/10.1084/jem.20071087.

20. Wu, X., Briseño, C.G., Durai, V., Albring, J.C., Haldar, M., Bagadia, P., Kim, K.W., Randolph, G.J., Murphy, T.L., and Murphy, K.M. (2016). Mafb lineage tracing to distinguish macrophages from other immune lineages reveals dual identity of Langerhans cells. J. Exp. Med. *213*, 2553–2565. https://doi.org/10.1084/jem.20160600.

21. Bergamaschi, C., Stravokefalou, V., Stellas, D., Karaliota, S., Felber, B.K., and Pavlakis, G.N. (2021). Heterodimeric IL-15 in cancer immunotherapy. Cancers *13*, 837. https://doi.org/10.3390/cancers13040837.

22. Waldmann, T.A. (2006). The biology of interleukin-2 and interleukin-15: implications for cancer therapy and vaccine design. Nat. Rev. Immunol. *6*, 595–601. https://doi.org/10.1038/nri1901.

23. Waldmann, T.A., Miljkovic, M.D., and Conlon, K.C. (2020). Interleukin-15 (dys)regulation of lymphoid homeostasis: implications for therapy of autoimmunity and cancer. J. Exp. Med. *217*, e20191062. https://doi.org/10.1084/jem.20191062.

24. Ng, S.S.M., Nagy, B.A., Jensen, S.M., Hu, X., Alicea, C., Fox, B.A., Felber, B.K., Bergamaschi, C., and Pavlakis, G.N. (2017). Heterodimeric IL15 treatment enhances tumor infiltration, persistence, and effector functions of adoptively transferred tumor-specific T cells in the absence of lymphodepletion. Clin. Cancer Res. *23*, 2817–2830. https://doi.org/10.1158/1078-0432.Ccr-16-1808.

25. Berard, M., Brandt, K., Bulfone-Paus, S., and Tough, D.F. (2003). IL-15 promotes the survival of naive and memory phenotype CD8+ T cells. J. Immunol. *170*, 5018–5026. https://doi.org/10.4049/jimmunol.170.10.5018.

26. Carson, W.E., Giri, J.G., Lindemann, M.J., Linett, M.L., Ahdieh, M., Paxton, R., Anderson, D., Eisenmann, J., Grabstein, K., and Caligiuri, M.A. (1994). Interleukin (IL) 15 is a novel cytokine that activates human natural killer cells via components of the IL-2 receptor. J. Exp. Med. *180*, 1395–1403.

27. Klebanoff, C.A., Finkelstein, S.E., Surman, D.R., Lichtman, M.K., Gattinoni, L., Theoret, M.R., Grewal, N., Spiess, P.J., Antony, P.A., Palmer, D.C., et al. (2004). IL-15 enhances the in vivo antitumor activity of tumor-reactive CD8+ T cells. Proc. Natl. Acad. Sci. USA *101*, 1969–1974. https://doi.org/10.1073/pnas.0307298101.

28. Bergamaschi, C., Pandit, H., Nagy, B.A., Stellas, D., Jensen, S.M., Bear, J., Cam, M., Valentin, A., Fox, B.A., Felber, B.K., and Pavlakis, G.N. (2020). Heterodimeric IL-15 delays tumor growth and promotes intratumoral CTL and dendritic cell accumulation by a cytokine network involving XCL1, IFN-gamma, CXCL9 and CXCL10. J. Immunother. Cancer *8*, e000599. https://doi.org/10.1136/jitc-2020-000599.

29. Mathios, D., Park, C.K., Marcus, W.D., Alter, S., Rhode, P.R., Jeng, E.K., Wong, H.C., Pardoll, D.M., and Lim, M. (2016). Therapeutic administration of IL-15 superagonist complex ALT-803 leads to long-term survival and durable antitumor immune response in a murine glioblastoma model. Int. J. Cancer *138*, 187–194. https://doi.org/10.1002/ijc.29686.

30. Xu, W., Jones, M., Liu, B., Zhu, X., Johnson, C.B., Edwards, A.C., Kong, L., Jeng, E.K., Han, K., Marcus, W.D., et al. (2013). Efficacy and mechanism-of-action of a novel superagonist interleukin-15: interleukin-15 receptor alphaSu/Fc fusion complex in syngeneic murine models of multiple myeloma. Cancer Res. *73*, 3075–3086. https://doi.org/10.1158/0008-5472.CAN-12-2357.

31. Yu, P., Steel, J.C., Zhang, M., Morris, J.C., Waitz, R., Fasso, M., Allison, J.P., and Waldmann, T.A. (2012). Simultaneous inhibition of two regulatory T-cell subsets enhanced Interleukin-15 efficacy in a prostate tumor model. Proc. Natl. Acad. Sci. USA *109*, 6187–6192. https://doi.org/10.1073/pnas.1203479109.

32. Yu, P., Steel, J.C., Zhang, M., Morris, J.C., and Waldmann, T.A. (2010). Simultaneous blockade of multiple immune system inhibitory checkpoints enhances antitumor activity mediated by interleukin-15 in a murine metastatic colon carcinoma model. Clin. Cancer Res. *16*, 6019–6028. https://doi.org/10.1158/1078-0432.CCR-10-1966.

33. Conlon, K., Watson, D.C., Waldmann, T.A., Valentin, A., Bergamaschi, C., Felber, B.K., Peer, C.J., Figg, W.D., Potter, E.L., Roederer, M., et al. (2021). Phase I study of single agent NIZ985, a recombinant heterodimeric IL-15 agonist, in adult patients with metastatic or unresectable solid tumors. J. Immunother. Cancer *9*, e003388. https://doi.org/10.1136/jitc-2021-003388.

34. Conlon, K.C., Lugli, E., Welles, H.C., Rosenberg, S.A., Fojo, A.T., Morris, J.C., Fleisher, T.A., Dubois, S.P., Perera, L.P., Stewart, D.M., et al. (2015). Redistribution, hyperproliferation, activation of natural killer cells and CD8 T cells, and cytokine production during first-in-human clinical trial of recombinant human interleukin-15 in patients with cancer. J. Clin. Oncol. *33*, 74–82. https://doi.org/10.1200/JCO.2014.57.3329.

35. Conlon, K.C., Potter, E.L., Pittaluga, S., Lee, C.C.R., Miljkovic, M.D., Fleisher, T.A., Dubois, S., Bryant, B.R., Petrus, M., Perera, L.P., et al. (2019). IL15 by continuous intravenous infusion to adult patients with solid tumors in a phase I trial induced dramatic NK-cell subset expansion. Clin. Cancer Res. *25*, 4945–4954. https://doi.org/10.1158/1078-0432.CCR-18-3468.

36. Cooley, S., He, F., Bachanova, V., Vercellotti, G.M., DeFor, T.E., Curtsinger, J.M., Robertson, P., Grzywacz, B., Conlon, K.C., Waldmann, T.A., et al. (2019). First-in-human trial of rhIL-15 and haploidentical natural killer cell therapy for advanced acute myeloid leukemia. Blood Adv. *3*, 1970–1980. https://doi.org/10.1182/bloodadvances.2018028332.

37. Margolin, K., Morishima, C., Velcheti, V., Miller, J.S., Lee, S.M., Silk, A.W., Holtan, S.G., Lacroix, A.M., Fling, S.P., Kaiser, J.C., et al. (2018). Phase I trial of ALT-803, A novel recombinant IL15 complex, in patients

with advanced solid tumors. Clin. Cancer Res. *24*, 5552–5561. https://doi.org/10.1158/1078-0432.CCR-18-0945.

38. Miller, J.S., Morishima, C., McNeel, D.G., Patel, M.R., Kohrt, H.E.K., Thompson, J.A., Sondel, P.M., Wakelee, H.A., Disis, M.L., Kaiser, J.C., et al. (2018). A first-in-human phase I study of subcutaneous outpatient recombinant human IL15 (rhIL15) in adults with advanced solid tumors. Clin. Cancer Res. *24*, 1525–1535. https://doi.org/10.1158/1078-0432.CCR-17-2451.

39. Romee, R., Cooley, S., Berrien-Elliott, M.M., Westervelt, P., Verneris, M.R., Wagner, J.E., Weisdorf, D.J., Blazar, B.R., Ustun, C., DeFor, T.E., et al. (2018). First-in-human phase 1 clinical study of the IL-15 superagonist complex ALT-803 to treat relapse after transplantation. Blood *131*, 2515–2527. https://doi.org/10.1182/blood-2017-12-823757.

40. Bergamaschi, C., Jalah, R., Kulkarni, V., Rosati, M., Zhang, G.M., Alicea, C., Zolotukhin, A.S., Felber, B.K., and Pavlakis, G.N. (2009). Secretion and biological activity of short signal peptide IL-15 is chaperoned by IL-15 receptor alpha in vivo. J. Immunol. *183*, 3064–3072. https://doi.org/10.4049/jimmunol.0900693.

41. Bergamaschi, C., Rosati, M., Jalah, R., Valentin, A., Kulkarni, V., Alicea, C., Zhang, G.M., Patel, V., Felber, B.K., and Pavlakis, G.N. (2008). Intracellular interaction of interleukin-15 with its receptor {alpha} during production leads to mutual stabilization and increased bioactivity. J. Biol. Chem. *283*, 4189–4199.

42. Bergamaschi, C., Bear, J., Rosati, M., Beach, R.K., Alicea, C., Sowder, R., Chertova, E., Rosenberg, S.A., Felber, B.K., and Pavlakis, G.N. (2012). Circulating IL-15 exists as heterodimeric complex with soluble IL-15Ralpha in human and mouse serum. Blood *120*, e1–e8. https://doi.org/10.1182/blood-2011-10-384362.

43. Chertova, E., Bergamaschi, C., Chertov, O., Sowder, R., Bear, J., Roser, J.D., Beach, R.K., Lifson, J.D., Felber, B.K., and Pavlakis, G.N. (2013). Characterization and favorable in vivo properties of heterodimeric soluble IL-15.IL-15Ralpha cytokine compared to IL-15 monomer. J. Biol. Chem. *288*, 18093–18103. https://doi.org/10.1074/jbc.M113.461756.

44. Bottcher, J.P., Bonavita, E., Chakravarty, P., Blees, H., Cabeza-Cabrerizo, M., Sammicheli, S., Rogers, N.C., Sahai, E., Zelenay, S., and Reis, E.S.C. (2018). NK cells stimulate recruitment of cDC1 into the tumor microenvironment promoting cancer immune control. Cell *172*, 1022–1037. https://doi.org/10.1016/j.cell.2018.01.004.

45. Schlitzer, A., McGovern, N., Teo, P., Zelante, T., Atarashi, K., Low, D., Ho, A.W.S., See, P., Shin, A., Wasan, P.S., et al. (2013). IRF4 transcription factor-dependent CD11b+ dendritic cells in human and mouse control mucosal IL-17 cytokine responses. Immunity *38*, 970–983. https://doi.org/10.1016/j.immuni.2013.04.011.

46. Qu, C., Brinck-Jensen, N.S., Zang, M., and Chen, K. (2014). Monocyte-derived dendritic cells: targets as potent antigen-presenting cells for the design of vaccines against infectious diseases. Int. J. Infect. Dis. *19*, 1–5. https://doi.org/10.1016/j.ijid.2013.09.023.

47. Kim, T.S., Gorski, S.A., Hahn, S., Murphy, K.M., and Braciale, T.J. (2014). Distinct dendritic cell subsets dictate the fate decision between effector and memory CD8(+) T cell differentiation by a CD24-dependent mechanism. Immunity *40*, 400–413. https://doi.org/10.1016/j.immuni.2014.02.004.

48. Persson, E.K., Scott, C.L., Mowat, A.M., and Agace, W.W. (2013). Dendritic cell subsets in the intestinal lamina propria: ontogeny and function. Eur. J. Immunol. *43*, 3098–3107. https://doi.org/10.1002/eji.201343740.

49. Bain, C.C., Montgomery, J., Scott, C.L., Kel, J.M., Girard-Madoux, M.J.H., Martens, L., Zangerle-Murray, T.F.P., Ober-Blöbaum, J., Lindenbergh-Kortleve, D., Samsom, J.N., et al. (2017). TGFbetaR signalling controls CD103(+)CD11b(+) dendritic cell development in the intestine. Nat. Commun. *8*, 620. https://doi.org/10.1038/s41467-017-00658-6.

50. Brown, C.C., Gudjonson, H., Pritykin, Y., Deep, D., Lavallée, V.P., Mendoza, A., Fromme, R., Mazutis, L., Ariyan, C., Leslie, C., et al. (2019). Transcriptional basis of mouse and human dendritic cell heterogeneity. Cell *179*, 846–863. https://doi.org/10.1016/j.cell.2019.09.035.

51. Kaczanowska, S., Beury, D.W., Gopalan, V., Tycko, A.K., Qin, H., Clements, M.E., Drake, J., Nwanze, C., Murgai, M., Rae, Z., et al. (2021). Genetically engineered myeloid cells rebalance the core immune suppression program in metastasis. Cell *184*, 2033–2052. https://doi.org/10.1016/j.cell.2021.02.048.

52. Theisen, D.J., Davidson, J.T., 4th, Briseño, C.G., Gargaro, M., Lauron, E.J., Wang, Q., Desai, P., Durai, V., Bagadia, P., Brickner, J.R., et al. (2018). WDFY4 is required for cross-presentation in response to viral and tumor antigens. Science *362*, 694–699. https://doi.org/10.1126/science.aat5030.

53. Santambrogio, L., Berendam, S.J., and Engelhard, V.H. (2019). The antigen processing and presentation machinery in lymphatic endothelial cells. Front. Immunol. *10*, 1033. https://doi.org/10.3389/fimmu.2019.01033.

54. Hao, Y., Hao, S., Andersen-Nissen, E., Mauck, W.M., 3rd, Zheng, S., Butler, A., Lee, M.J., Wilk, A.J., Darby, C., Zager, M., et al. (2021). Integrated analysis of multimodal single-cell data. Cell *184*, 3573–3587. https://doi.org/10.1016/j.cell.2021.04.048.

55. Blondel, V.D., Guillaume, J.L., Lambiotte, R., and Lefebvre, E. (2008). Fast unfolding of communities in large networks. J. Stat. Mech. *2008*, P10008. https://doi.org/10.1088/1742-5468/2008/10/P10008.

56. Tzelepis, F., Verway, M., Daoud, J., Gillard, J., Hassani-Ardakani, K., Dunn, J., Downey, J., Gentile, M.E., Jaworska, J., Sanchez, A.M.J., et al. (2015). Annexin1 regulates DC efferocytosis and cross-presentation during Mycobacterium tuberculosis infection. J. Clin. Invest. *125*, 752–768. https://doi.org/10.1172/JCI77014.

57. Toyonaga, K., Torigoe, S., Motomura, Y., Kamichi, T., Hayashi, J.M., Morita, Y.S., Noguchi, N., Chuma, Y., Kiyohara, H., Matsuo, K., et al. (2016). C-type lectin receptor DCAR recognizes mycobacterial phosphatidyl-inositol mannosides to promote a Th1 response during infection. Immunity *45*, 1245–1257. https://doi.org/10.1016/j.immuni.2016.10.012.

58. Napoletano, C., Rughetti, A., Agervig Tarp, M.P., Coleman, J., Bennett, E.P., Picco, G., Sale, P., Denda-Nagai, K., Irimura, T., Mandel, U., et al. (2007). Tumor-associated Tn-MUC1 glycoform is internalized through the macrophage galactose-type C-type lectin and delivered to the HLA class I and II compartments in dendritic cells. Cancer Res. *67*, 8358–8367. https://doi.org/10.1158/0008-5472.CAN-07-1035.

59. Kis-Toth, K., Bacskai, I., Gogolak, P., Mazlo, A., Szatmari, I., and Rajnavolgyi, E. (2013). Monocyte-derived dendritic cell subpopulations use different types of matrix metalloproteinases inhibited by GM6001. Immunobiology *218*, 1361–1369. https://doi.org/10.1016/j.imbio.2013.06.012.

60. Bonnardel, J., Da Silva, C., Henri, S., Tamoutounour, S., Chasson, L., Montañana-Sanchis, F., Gorvel, J.P., and Lelouard, H. (2015). Innate and adaptive immune functions of peyer's patch monocyte-derived cells. Cell Rep. *11*, 770–784. https://doi.org/10.1016/j.celrep.2015.03.067.

61. Le Naour, F., Hohenkirk, L., Grolleau, A., Misek, D.E., Lescure, P., Geiger, J.D., Hanash, S., and Beretta, L. (2001). Profiling changes in gene expression during differentiation and maturation of monocyte-derived dendritic cells using both oligonucleotide microarrays and proteomics. J. Biol. Chem. *276*, 17920–17931. https://doi.org/10.1074/jbc.M100156200.

62. Ashburner, M., Ball, C.A., Blake, J.A., Botstein, D., Butler, H., Cherry, J.M., Davis, A.P., Dolinski, K., Dwight, S.S., Eppig, J.T., et al. (2000). Gene ontology: tool for the unification of biology. The Gene Ontology Consortium. Nat. Genet. *25*, 25–29. https://doi.org/10.1038/75556.

63. Gene Ontology Consortium (2021). The Gene Ontology resource: enriching a GOld mine. Nucleic Acids Res. *49*, D325–D334. https://doi.org/10.1093/nar/gkaa1113.

64. Lindstedt, M., Johansson-Lindbom, B., and Borrebaeck, C.A.K. (2002). Global reprogramming of dendritic cells in response to a concerted action of inflammatory mediators. Int. Immunol. *14*, 1203–1213. https://doi.org/10.1093/intimm/dxf082.

65. Shaffer, A.L., Emre, N.C.T., Lamy, L., Ngo, V.N., Wright, G., Xiao, W., Powell, J., Dave, S., Yu, X., Zhao, H., et al. (2008). IRF4 addiction in multiple myeloma. Nature *454*, 226–231. https://doi.org/10.1038/nature07064.

66. Stravokefalou, V., Stellas, D., Karaliota, S., Nagy, B.A., Valentin, A., Bergamaschi, C., Dimas, K., and Pavlakis, G.N. (2022). Heterodimeric IL-15 (hetIL-15) reduces circulating tumor cells and metastasis formation improving chemotherapy and surgery in 4T1 mouse model of TNBC. Front. Immunol. *13*, 1014802. https://doi.org/10.3389/fimmu.2022.1014802.

67. Marabelle, A., Kohrt, H., Caux, C., and Levy, R. (2014). Intratumoral immunization: a new paradigm for cancer therapy. Clin. Cancer Res. *20*, 1747–1756. https://doi.org/10.1158/1078-0432.CCR-13-2116.

68. Champiat, S., Tselikas, L., Farhane, S., Raoult, T., Texier, M., Lanoy, E., Massard, C., Robert, C., Ammari, S., De Baère, T., and Marabelle, A. (2021). Intratumoral immunotherapy: from trial design to clinical practice. Clin. Cancer Res. *27*, 665–679. https://doi.org/10.1158/1078-0432.CCR-20-0473.

69. Kurz, E., Hirsch, C.A., Dalton, T., Shadaloey, S.A., Khodadadi-Jamayran, A., Miller, G., Pareek, S., Rajaei, H., Mohindroo, C., Baydogan, S., et al. (2022). Exercise-induced engagement of the IL-15/I-15Rα axis promotes anti-tumor immunity in pancreatic cancer. Cancer Cell *40*, 720–737.e5. https://doi.org/10.1016/j.ccell.2022.05.006.

70. Waldmann, T.A., Lugli, E., Roederer, M., Perera, L.P., Smedley, J.V., Macallister, R.P., Goldman, C.K., Bryant, B.R., Decker, J.M., Fleisher, T.A., et al. (2011). Safety (toxicity), pharmacokinetics, immunogenicity, and impact on elements of the normal immune system of recombinant human IL-15 in rhesus macaques. Blood *117*, 4787–4795. https://doi.org/10.1182/blood-2010-10-311456.

71. Berger, C., Berger, M., Hackman, R.C., Gough, M., Elliott, C., Jensen, M.C., and Riddell, S.R. (2009). Safety and immunologic effects of IL-15 administration in nonhuman primates. Blood *114*, 2417–2426. https://doi.org/10.1182/blood-2008-12-189266.

72. Dubois, S.P., Waldmann, T.A., and Müller, J.R. (2005). Survival adjustment of mature dendritic cells by IL-15. Proc. Natl. Acad. Sci. USA *102*, 8662–8667. https://doi.org/10.1073/pnas.0503360102.

73. Mattei, F., Schiavoni, G., Belardelli, F., and Tough, D.F. (2001). IL-15 is expressed by dendritic cells in response to type I IFN, double-stranded RNA, or lipopolysaccharide and promotes dendritic cell activation. J. Immunol. *167*, 1179–1187. https://doi.org/10.4049/jimmunol.167.3.1179.

74. Saikh, K.U., Khan, A.S., Kissner, T., and Ulrich, R.G. (2001). IL-15-induced conversion of monocytes to mature dendritic cells. Clin. Exp. Immunol. *126*, 447–455. https://doi.org/10.1046/j.1365-2249.2001.01672.x.

75. Saikh, K.U., Kissner, T.L., Nystrom, S., Ruthel, G., and Ulrich, R.G. (2008). Interleukin-15 increases vaccine efficacy through a mechanism linked to dendritic cell maturation and enhanced antibody titers. Clin. Vaccine Immunol. *15*, 131–137. https://doi.org/10.1128/CVI.00320-07.

76. Tourkova, I.L., Shurin, G.V., Chatta, G.S., Perez, L., Finke, J., Whiteside, T.L., Ferrone, S., and Shurin, M.R. (2005). Restoration by IL-15 of MHC class I antigen-processing machinery in human dendritic cells inhibited by tumor-derived gangliosides. J. Immunol. *175*, 3045–3052. https://doi.org/10.4049/jimmunol.175.5.3045.

77. Tourkova, I.L., Yurkovetsky, Z.R., Gambotto, A., Makarenkova, V.P., Perez, L., Balkir, L., Robbins, P.D., Shurin, M.R., and Shurin, G.V. (2002). Increased function and survival of IL-15-transduced human dendritic cells are mediated by up-regulation of IL-15Ralpha and Bcl-2. J. Leukoc. Biol. *72*, 1037–1045.

78. Alferink, J., Lieberam, I., Reindl, W., Behrens, A., Weiss, S., Hüser, N., Gerauer, K., Ross, R., Reske-Kunz, A.B., Ahmad-Nejad, P., et al. (2003). Compartmentalized production of CCL17 in vivo: strong inducibility in peripheral dendritic cells contrasts selective absence from the spleen. J. Exp. Med. *197*, 585–599. https://doi.org/10.1084/jem.20021859.

79. Guilliams, M., Ginhoux, F., Jakubzick, C., Naik, S.H., Onai, N., Schraml, B.U., Segura, E., Tussiwand, R., and Yona, S. (2014). Dendritic cells, monocytes and macrophages: a unified nomenclature based on ontogeny. Nat. Rev. Immunol. *14*, 571–578. https://doi.org/10.1038/nri3712.

80. Sheng, J., Chen, Q., Soncin, I., Ng, S.L., Karjalainen, K., and Ruedl, C. (2017). A discrete subset of monocyte-derived cells among typical conventional type 2 dendritic cells can efficiently cross-present. Cell Rep. *21*, 1203–1214. https://doi.org/10.1016/j.celrep.2017.10.024.

81. Calabro, S., Liu, D., Gallman, A., Nascimento, M.S.L., Yu, Z., Zhang, T.T., Chen, P., Zhang, B., Xu, L., Gowthaman, U., et al. (2016). Differential intrasplenic migration of dendritic cell subsets tailors adaptive immunity. Cell Rep. *16*, 2472–2485. https://doi.org/10.1016/j.celrep.2016.07.076.

82. Sichien, D., Scott, C.L., Martens, L., Vanderkerken, M., Van Gassen, S., Plantinga, M., Joeris, T., De Prijck, S., Vanhoutte, L., Vanheerswynghels, M., et al. (2016). IRF8 transcription factor controls survival and function of terminally differentiated conventional and plasmacytoid dendritic cells, respectively. Immunity *45*, 626–640. https://doi.org/10.1016/j.immuni.2016.08.013.

83. Feng, F., Wang, Y.C., Hu, X.B., Liu, X.W., Ji, G., Chen, Y.R., Wang, L., He, F., Dou, G.R., Liang, L., et al. (2010). The transcription factor RBP-J-mediated signaling is essential for dendritic cells to evoke efficient anti-tumor immune responses in mice. Mol. Cancer *9*, 90. https://doi.org/10.1186/1476-4598-9-90.

84. Spranger, S., Dai, D., Horton, B., and Gajewski, T.F. (2017). Tumor-residing Batf3 dendritic cells are required for effector T cell trafficking and adoptive T cell therapy. Cancer Cell *31*, 711–723. https://doi.org/10.1016/j.ccell.2017.04.003.

85. Karsunky, H., Merad, M., Cozzio, A., Weissman, I.L., and Manz, M.G. (2003). Flt3 ligand regulates dendritic cell development from Flt3+ lymphoid and myeloid-committed progenitors to Flt3+ dendritic cells in vivo. J. Exp. Med. *198*, 305–313. https://doi.org/10.1084/jem.20030323.

86. Bosteels, C., Neyt, K., Vanheerswynghels, M., van Helden, M.J., Sichien, D., Debeuf, N., De Prijck, S., Bosteels, V., Vandamme, N., Martens, L., et al. (2020). Inflammatory type 2 cDCs acquire features of cDC1s and macrophages to orchestrate immunity to respiratory virus infection. Immunity *52*, 1039–1056. https://doi.org/10.1016/j.immuni.2020.04.005.

87. Diao, J., Gu, H., Tang, M., Zhao, J., and Cattral, M.S. (2018). Tumor dendritic cells (DCs) derived from precursors of conventional DCs are dispensable for intratumor CTL responses. J. Immunol. *201*, 1306–1314. https://doi.org/10.4049/jimmunol.1701514.

88. Kenkel, J.A., Tseng, W.W., Davidson, M.G., Tolentino, L.L., Choi, O., Bhattacharya, N., Seeley, E.S., Winer, D.A., Reticker-Flynn, N.E., and Engleman, E.G. (2017). An immunosuppressive dendritic cell subset accumulates at secondary sites and promotes metastasis in pancreatic cancer. Cancer Res. *77*, 4158–4170. https://doi.org/10.1158/0008-5472.CAN-16-2212.

89. Bain, C.C., Scott, C.L., Uronen-Hansson, H., Gudjonsson, S., Jansson, O., Grip, O., Guilliams, M., Malissen, B., Agace, W.W., and Mowat, A.M. (2013). Resident and pro-inflammatory macrophages in the colon represent alternative context-dependent fates of the same Ly6Chi monocyte precursors. Mucosal Immunol. *6*, 498–510. https://doi.org/10.1038/mi.2012.89.

90. Tamoutounour, S., Henri, S., Lelouard, H., de Bovis, B., de Haar, C., van der Woude, C.J., Woltman, A.M., Reyal, Y., Bonnet, D., Sichien, D., et al. (2012). CD64 distinguishes macrophages from dendritic cells in the gut and reveals the Th1-inducing role of mesenteric lymph node macrophages during colitis. Eur. J. Immunol. *42*, 3150–3166. https://doi.org/10.1002/eji.201242847.

91. Zigmond, E., Varol, C., Farache, J., Elmaliah, E., Satpathy, A.T., Friedlander, G., Mack, M., Shpigel, N., Boneca, I.G., Murphy, K.M., et al. (2012). Ly6C hi monocytes in the inflamed colon give rise to proinflammatory effector cells and migratory antigen-presenting cells. Immunity *37*, 1076–1090. https://doi.org/10.1016/j.immuni.2012.08.026.

92. Wakim, L.M., Waithman, J., van Rooijen, N., Heath, W.R., and Carbone, F.R. (2008). Dendritic cell-induced memory T cell activation in nonlymphoid tissues. Science *319*, 198–202. https://doi.org/10.1126/science.1151869.

93. Nakano, H., Lin, K.L., Yanagita, M., Charbonneau, C., Cook, D.N., Kakiuchi, T., and Gunn, M.D. (2009). Blood-derived inflammatory dendritic cells in lymph nodes stimulate acute T helper type 1 immune responses. Nat. Immunol. *10*, 394–402. https://doi.org/10.1038/ni.1707.

94. Le Borgne, M., Etchart, N., Goubier, A., Lira, S.A., Sirard, J.C., van Rooijen, N., Caux, C., Aït-Yahia, S., Vicari, A., Kaiserlian, D., and Dubois, B. (2006). Dendritic cells rapidly recruited into epithelial tissues via CCR6/CCL20 are responsible for CD8+ T cell crosspriming in vivo. Immunity *24*, 191–201. https://doi.org/10.1016/j.immuni.2006.01.005.

95. Kobayashi, H., Watanabe, R., and Choyke, P.L. (2013). Improving conventional enhanced permeability and retention (EPR) effects; what is the appropriate target? Theranostics *4*, 81–89. https://doi.org/10.7150/thno.7193.

96. Lee, J.Y., Kim, H., Cha, M.Y., Park, H.G., Kim, Y.J., Kim, I.Y., and Kim, J.M. (2009). Clostridium difficile toxin A promotes dendritic cell maturation and chemokine CXCL2 expression through p38, IKK, and the NF-kappaB signaling pathway. J. Mol. Med. *87*, 169–180. https://doi.org/10.1007/s00109-008-0415-2.

97. Eberlein, J., Nguyen, T.T., Victorino, F., Golden-Mason, L., Rosen, H.R., and Homann, D. (2010). Comprehensive assessment of chemokine expression profiles by flow cytometry. J. Clin. Invest. *120*, 907–923. https://doi.org/10.1172/JCI40645.

98. Henry, C.J., Ornelles, D.A., Mitchell, L.M., Brzoza-Lewis, K.L., and Hiltbold, E.M. (2008). IL-12 produced by dendritic cells augments CD8+ T cell activation through the production of the chemokines CCL1 and CCL17. J. Immunol. *181*, 8576–8584. https://doi.org/10.4049/jimmunol.181.12.8576.

99. McColl, S.R. (2002). Chemokines and dendritic cells: a crucial alliance. Immunol. Cell Biol. *80*, 489–496. https://doi.org/10.1046/j.1440-1711.2002.01113.x.

100. Semmling, V., Lukacs-Kornek, V., Thaiss, C.A., Quast, T., Hochheiser, K., Panzer, U., Rossjohn, J., Perlmutter, P., Cao, J., Godfrey, D.I., et al. (2010). Alternative cross-priming through CCL17-CCR4-mediated attraction of CTLs toward NKT cell-licensed DCs. Nat. Immunol. *11*, 313–320. https://doi.org/10.1038/ni.1848.

101. Shin, H., Kumamoto, Y., Gopinath, S., and Iwasaki, A. (2016). CD301b+ dendritic cells stimulate tissue-resident memory CD8+ T cells to protect against genital HSV-2. Nat. Commun. *7*, 13346. https://doi.org/10.1038/ncomms13346.

102. Denda-Nagai, K., Aida, S., Saba, K., Suzuki, K., Moriyama, S., Oo-Puthinan, S., Tsuiji, M., Morikawa, A., Kumamoto, Y., Sugiura, D., et al. (2010). Distribution and function of macrophage galactose-type C-type lectin 2 (MGL2/CD301b): efficient uptake and presentation of glycosylated antigens by dendritic cells. J. Biol. Chem. *285*, 19193–19204. https://doi.org/10.1074/jbc.M110.113613.

103. Heger, L., Balk, S., Lühr, J.J., Heidkamp, G.F., Lehmann, C.H.K., Hatscher, L., Purbojo, A., Hartmann, A., Garcia-Martin, F., Nishimura, S.I., et al. (2018). CLEC10A is a specific marker for human CD1c(+) dendritic cells and enhances their toll-like receptor 7/8-induced cytokine secretion. Front. Immunol. *9*, 744. https://doi.org/10.3389/fimmu.2018.00744.

104. Nizzoli, G., Krietsch, J., Weick, A., Steinfelder, S., Facciotti, F., Gruarin, P., Bianco, A., Steckel, B., Moro, M., Crosti, M., et al. (2013). Human CD1c+ dendritic cells secrete high levels of IL-12 and potently prime cytotoxic T-cell responses. Blood *122*, 932–942. https://doi.org/10.1182/blood-2013-04-495424.

105. Schreibelt, G., Bol, K.F., Westdorp, H., Wimmers, F., Aarntzen, E.H.J.G., Duiveman-de Boer, T., van de Rakt, M.W.M.M., Scharenborg, N.M., de Boer, A.J., Pots, J.M., et al. (2016). Effective clinical responses in metastatic melanoma patients after vaccination with primary myeloid dendritic cells. Clin. Cancer Res. *22*, 2155–2166. https://doi.org/10.1158/1078-0432.CCR-15-2205.

106. Tel, J., Aarntzen, E.H.J.G., Baba, T., Schreibelt, G., Schulte, B.M., Benitez-Ribas, D., Boerman, O.C., Croockewit, S., Oyen, W.J.G., van Rossum, M., et al. (2013). Natural human plasmacytoid dendritic cells induce antigen-specific T-cell responses in melanoma patients. Cancer Res. *73*, 1063–1075. https://doi.org/10.1158/0008-5472.CAN-12-2583.

107. Westdorp, H., Creemers, J.H.A., van Oort, I.M., Schreibelt, G., Gorris, M.A.J., Mehra, N., Simons, M., de Goede, A.L., van Rossum, M.M., Croockewit, A.J., et al. (2019). Blood-derived dendritic cell vaccinations induce immune responses that correlate with clinical outcome in patients with chemo-naive castration-resistant prostate cancer. J. Immunother. Cancer *7*, 302. https://doi.org/10.1186/s40425-019-0787-6.

108. Bell, D., Chomarat, P., Broyles, D., Netto, G., Harb, G.M., Lebecque, S., Valladeau, J., Davoust, J., Palucka, K.A., and Banchereau, J. (1999). In breast carcinoma tissue, immature dendritic cells reside within the tumor, whereas mature dendritic cells are located in peritumoral areas. J. Exp. Med. *190*, 1417–1426. https://doi.org/10.1084/jem.190.10.1417.

109. Lin, J.H., Huffman, A.P., Wattenberg, M.M., Walter, D.M., Carpenter, E.L., Feldser, D.M., Beatty, G.L., Furth, E.E., and Vonderheide, R.H. (2020). Type 1 conventional dendritic cells are systemically dysregulated early in pancreatic carcinogenesis. J. Exp. Med. *217*, e20190673. https://doi.org/10.1084/jem.20190673.

110. Hänzelmann, S., Castelo, R., and Guinney, J. (2013). GSVA: gene set variation analysis for microarray and RNA-seq data. BMC Bioinf. *14*, 7. https://doi.org/10.1186/1471-2105-14-7.

111. Liberzon, A., Birger, C., Thorvaldsdóttir, H., Ghandi, M., Mesirov, J.P., and Tamayo, P. (2015). The Molecular Signatures Database (MSigDB) hallmark gene set collection. Cell Syst. *1*, 417–425. https://doi.org/10.1016/j.cels.2015.12.004.

112. Subramanian, A., Tamayo, P., Mootha, V.K., Mukherjee, S., Ebert, B.L., Gillette, M.A., Paulovich, A., Pomeroy, S.L., Golub, T.R., Lander, E.S., and Mesirov, J.P. (2005). Gene set enrichment analysis: a knowledge-based approach for interpreting genome-wide expression profiles. Proc. Natl. Acad. Sci. USA *102*, 15545–15550. https://doi.org/10.1073/pnas.0506580102.

113. Finak, G., McDavid, A., Yajima, M., Deng, J., Gersuk, V., Shalek, A.K., Slichter, C.K., Miller, H.W., McElrath, M.J., Prlic, M., et al. (2015). MAST: a flexible statistical framework for assessing transcriptional changes and characterizing heterogeneity in single-cell RNA sequencing data. Genome Biol. *16*, 278. https://doi.org/10.1186/s13059-015-0844-5.

114. Danaher, P., Warren, S., Dennis, L., D'Amico, L., White, A., Disis, M.L., Geller, M.A., Odunsi, K., Beechem, J., and Fling, S.P. (2017). Gene expression markers of tumor infiltrating leukocytes. J. Immunother. Cancer *5*, 18. https://doi.org/10.1186/s40425-017-0215-8.

115. Kleinman, H.K., and Martin, G.R. (2005). Matrigel: basement membrane matrix with biological activity. Semin. Cancer Biol. *15*, 378–386. https://doi.org/10.1016/j.semcancer.2005.05.004.

116. Ritchie, M.E., Phipson, B., Wu, D., Hu, Y., Law, C.W., Shi, W., and Smyth, G.K. (2015). Limma powers differential expression analyses for RNA-sequencing and microarray studies. Nucleic Acids Res. *43*, e47. https://doi.org/10.1093/nar/gkv007.

117. Hafemeister, C., and Satija, R. (2019). Normalization and variance stabilization of single-cell RNA-seq data using regularized negative binomial regression. Genome Biol. *20*, 296. https://doi.org/10.1186/s13059-019-1874-1.

118. Aran, D., Looney, A.P., Liu, L., Wu, E., Fong, V., Hsu, A., Chak, S., Naikawadi, R.P., Wolters, P.J., Abate, A.R., et al. (2019). Reference-based analysis of lung single-cell sequencing reveals a transitional profibrotic macrophage. Nat. Immunol. *20*, 163–172. https://doi.org/10.1038/s41590-018-0276-y.

119. Benjamini, Y., and Hochberg, Y. (1995). Controlling the false discovery rate: a practical and powerful approach to multiple testing. J. Roy. Stat. Soc. B *57*, 289–300.

STAR★METHODS

KEY RESOURCES TABLE

REAGENT or RESOURCE	SOURCE	IDENTIFIER
Antibodies		
InVivoMAb anti-mouse NK1.1 (clone PK136)	BioXCell	Cat#BE0036; RRID:AB_1107737
InVivoMAb mouse IgG2a isotype control	BioXCell	Cat#BE0085; RRID:AB_1107771
CD8a Monoclonal Antibody (clone 4SM15)	eBioscience	Cat#14-0808-82; RRID:AB_2572861
Klrb1c/CD161c Rabbit Monoclonal Antibody (clone E6Y9G)	Cell Signaling	Cat#39197; RRID:AB_2892989
Isotype rat IgG2a antibody	BD Biosciences	Cat#559073; RRID:AB_479682
APC-Cy7 Rat Anti-Mouse CD45 (clone 30-F11)	BD Biosciences	Cat#557659; RRID:AB_396774
FITC anti-mouse CD45 Antibody (clone 30-F11)	Biolegend	Cat#103108; RRID:AB_312973
PE/Cyanine5 anti-mouse CD3ε Antibody (clone 145-2C11)	Biolegend	Cat#100310; RRID:AB_312675
PE Hamster Anti-Mouse CD3e (clone 145-2C11)	BD Biosciences	Cat#553064; RRID:AB_394597
PE/Cyanine5 anti-mouse NK-1.1 Antibody (clone PK136)	Biolegend	Cat#108716; RRID:AB_493590
BV650 Rat Anti-Mouse CD8a (clone 53–6.6)	BD Biosciences	Cat#563234; RRID:AB_2738084
V450 Rat Anti-Mouse CD335 (NKp46) (clone 29A1.4)	BD Biosciences	Cat#560763; RRID:AB_1727469
PE-Cyanine5 CD19 Monoclonal Antibody (clone 1D3)	eBioscience	Cat#15-0193-82; RRID:AB_10643270
V450 Mouse Anti-Mouse NK-1.1 (clone PK136)	BD Biosciences	Cat#560524; RRID:AB_657672
PE-Cy™5 Rat Anti-Mouse CD45R/B220 (clone RA3-6B2)	BD Biosciences	Cat#553091; RRID:AB_394621
PE anti-mouse/rat XCR1 Antibody (clone ZET)	Biolegend	Cat#148204; RRID:AB_2563843
Alexa Fluor® 488 Rat Anti-Mouse I-A/I-E (clone M5/114.15.2)	BD Biosciences	Cat#562352; RRID:AB_11151902)
Brilliant Violet 650™ anti-mouse I-A/I-E Antibody (clone M5/114.15.2)	Biolegend	Cat#107641; RRID:AB_2565975
CD11c Monoclonal Antibody (N418), Alexa Fluor™ 700, (clone N418)	eBioscience	Cat#56-0114-82; RRID:AB_493992
BV605 Rat Anti-Mouse CD24 (clone M1/69)	BD Biosciences	Cat#563060; RRID:AB_2737981
CD11c Monoclonal Antibody (N418), PE (clone N418)	eBioscience	Cat#12-0114-82; RRID:AB_465552
Brilliant Violet 421™ anti-mouse CD64 (FcγRI) Antibody (clone X55-5/7.1)	Biolegend	Cat#139309; RRID:AB_2562694
Brilliant Violet 650™ anti-mouse F4/80 Antibody (clone BM8)	Biolegend	Cat#123149; RRID:AB_2564589
PE-CF594 Rat Anti-Mouse CD103 (clone M290)	BD Biosciences	Cat#565849; RRID:AB_2739377
CD11b Monoclonal Antibody (M1/70), PerCP-Cyanine5.5, (clone M1/70)	eBioscience	Cat#45-0112-82; RRID:AB_953558
PE/Cyanine7 anti-mouse CD172a (SIRPα) Antibody (clone P84)	Biolegend	Cat#144008; RRID:AB_2563546
Alexa Fluor 700 ati-mouse Ly6C (clone HK1.4)	Biolegend	Cat#128024; RRID: AB_10643270_
CD354 (TREM-1) Monoclonal Antibody, eFluor™ 660, (clone TR3MBL1)	eBioscience	Cat#50-3541-82; RRID:AB_2574205
CD101 Monoclonal Antibody, PE-Cyanine7, (clone Moushi101)	eBioscience	Cat#25-1011-82; RRID:AB_2573378
Brilliant Violet 605™ anti-mouse CX3CR1 Antibody (clone SA011F11)	Biolegend	Cat#149027; RRID:AB_2565937

(*Continued on next page*)

Continued

REAGENT or RESOURCE	SOURCE	IDENTIFIER
Alexa Fluor 700 anti-mouse Ly-6C Antibody (clone HK1.4)	Biolegend	Cat#128024; RRID:AB_10643270
Anti-GP2 (Glycoprotein 2) (Mouse) monoclonal Antibody (clone 2F11-C3)	MBL	Cat#D278-3; RRID:AB_10598188
Alexa Fluor® 700 Mouse anti-Ki-67 (clone B56)	BD Biosciences	Cat#561277; RRID:AB_10611571
Granzyme B Monoclonal Antibody-APC (clone GB12)	Thermo Fisher (Invitrogen)	Cat#MHGB05; RRID:AB_1500190
IRF8 Monoclonal Antibody (V3GYWCH), APC, (clone V3GYWCH)	eBioscience	Cat#17-9852-82; RRID:AB_2573318
FITC Rat Anti-Mouse IFN-γ (clone XMG1.2)	BD Biosciences	Cat#554411; RRID:AB_395375
TotalSeq^{a}-B0212 anti-mouse CD24 Antibody (clone 51/69)	Biolegend	Cat#101847; RRID:AB_2832282
TruStain FcX (clone 93)	Biolegend	Cat#101320; RRID:AB_1574975
RNAscope® 2.5 LS Probe –Mm-CD24a-C1	ACD	Cat#432698
RNAscope® 2.5 LS Probe –Mm-Mgl2-O1	ACD	Cat#822908-C2
RNAscope® 2.5 LS Probe –Mm-Ccl17-C3	ACD	Cat#428498-C3
RNAscope LS Multiplex Fluorescent Assay	ACD	Cat#322800
RNAscope™ Protease III & Protease IV Reagents	ACD	Cat# 322340
RNAscope® 3-plex LS Multiplex Negative Control Probe	ACD	Cat# 320878
Chemicals, peptides, and recombinant proteins		
hetIL-15	In house	N/A
Matrigel	Corning Inc.	Cat#354234
Quizartinib (AC220)	LC Laboratories	Cat#Q-4747
Formalin Solution, neutral buffered, 10%	Sigma-Aldrich	Cat#HT501128
Foxp3/Transcription Factor Staining Buffer Set	eBioscience	Cat#00-5523-00
RLT Buffer	Qiagen	Cat#79216
Fetal bovine serum	Sigma-Aldrich	Cat#F2442
RPMI medium	Gibco	Cat#11875-093
Penicillin/Streptomycin	Lonza	Cat#DE17-602E
LIVE/DEAD™ Fixable Aqua Dead Cell Stain Kit	Thermo Fisher (Invitrogen)	Cat#L34965
Recombinant murine GM-CSF	Peprotech	Cat#315-03
Recombinant murine IL-2	Peprotech	Cat#212-12
Critical commercial assays		
770 immune-oncology related gene probes	Nanostring Technology	https://nanostring.com/products/ncounter-assays-panels/oncology/pancancer-immune-profiling/
NEBNext® Ultra™ II Directional RNA Library Prep Kit	New England Biolabs Inv	Cat#E7760 S/L
CD8a^{+}T cells isolation Kit	Miltenyi Biotec Inc.	Cat#130-104-075
Tumor dissociation kit	Miltenyi Biotec Inc	Cat #130-096-730
CD11c MicroBeads UltraPure, mouse	Miltenyi Biotec Inc.	Cat#130-108-338
RNeasy Midi Kit	Qiagen	Cat#75144
RNeasy Mini kit	Qiagen	Cat#74104
RNeasy Micro Plus	Qiagen	Cat#74034
RNase-Free DNase Set	Qiagen	Cat#79254
Chromium Next GEM Single Cell 3' Reagent Kits v3.1	10xGenomics	Cat#PN-1000121
TSA Plus Cyanine 5 Detection Kit	AKOYA Biosciences	Cat#NEL745001KT
TSA Plus Fluorescein Detection Kit	AKOYA Biosciences	Cat#NEL741001KT
TSA Plus Cyanine 3 Detection Kit	AKOYA Biosciences	Cat#NEL744001KT

(*Continued on next page*)

Continued

REAGENT or RESOURCE	SOURCE	IDENTIFIER
Deposited data		
Raw and processed bulk RNAseq data	This paper	GEO: GSE226932
Raw and processed single-cell CITE-seq data	This paper	GEO: GSE180695
nCounter data	This paper	Github: https://github.com/NCI-VB/pavlakis_TNBC_hetIL-15/blob/main/Workbook_2/nidap_downloads/count_table-20200210.204226.csv
Raw data	This paper	https://doi.org.10.17632/ctnpxxdgrt
Experimental models: Cell lines		
EO771 cancer cells	CH3BioSystems	Cat#940001
4T1 cancer cells	ATCC	Cat#CRL-2539
KPC cells	Dr. Serguei Kozlov, Center for Advanced Preclinical Research, Frederick National Laboratory for Cancer Research	N/A
Experimental models: Organisms/strains		
Mouse: C57BL/6NHsd mice	Envigo	Cat#4410F
Mouse: C57BL/6NHsd mice	Charles River Laboratory	Strain#027
Mouse: C57BL/6J mice	Jackson Laboratory	Strain#000664
Mouse: BALB/cAnNCrl mice	Charles River Laboratories	Strain#028
Mouse: B6.129S7-Rag1tm1Mom/J	Jackson Laboratory	Strain#002216
Software and algorithms		
Original code	This paper	https://zenodo.org/record/7775594#.ZCHimOzMKrM
FlowJo software (version 10.7.1)	Tree Star	N/A
FlowJo t-SNE plugin	Tree Star	N/A
NIH Integrated Data Analysis Platform	This paper	https://nidap.nih.gov/workspace
NanoString nCounter	ATRF	N/A
GraphPad Prism 9.2.0	GraphPad, CS, USA	N/A
CCBR Pipeliner	This paper	https://github.com/CCBR/Pipeliner
List2pathway Enrichment Analysis	This paper	https://github.com/CCBR/l2p
Seurat	Hao et al.[54]	https://satijalab.org/seurat/; v3.1.5
SingleR	Hänzelmann et al.[110]	https://bioconductor.org/packages/release/bioc/html/SingleR.html
GSVA	Liberzon et al.[111]	https://bioconductor.org/packages/release/bioc/html/GSVA.html
MSigDB	Subramanian et al.[112] and Finak et al.[113]	https://www.gsea-msigdb.org/gsea/msigdb/
Other		
Reference dataset for Nanostring	Danaher et al.[114]	Reference dataset for Nanostring
Reference dataset for scRNAseq	Brown et al.[50]	Reference dataset for scRNAseq
AutoMACS® Pro Separator	Miltenyi Biotec Inc.	N/A
GentleMACS™ Dissociator	Miltenyi Biotec Inc.	N/A
LSRFortessa Cell Analyzer	BD Biosciences	N/A
nCounter PanCancer Immune Profiling Panel	NanoString Technologies	https://nanostring.com/products/ncounter-assays-panels/oncology/pancancer-immune-profiling
Aperio ScanScope FL Scanner	Leica Biosystems	N/A
Bond RX auto-stainer	Leica Biosystems	N/A

RESOURCE AVAILABILITY

Lead contact

Resource and reagent request should be directed to the lead contact.

Materials availability

This study did not generate new unique reagents.

Data and code availability

- Bulk RNA-seq and single-cell CITE-seq data have been deposited at GEO under the SuperSeries GSE226948 and are publicly available as of the date of publication. Accession numbers for specific datasets are listed in the key resources table. Nanostring nCounter data have been deposited at github along with the code for this manuscript. The path to the input data is listed in the key resources table. Raw data from Figures 1B–1I, 3C–3F, 4A-4F, 7B, 7C, 7E, 7F, S1A and S1B were deposited at Mendeley at https://doi.org.10.17632/ctnpxxdgrt.
- All original code has been deposited at github (https://github.com/NCI-VB/pavlakis_TNBC_hetIL-15/tree/v1.0.0) and is publicly available as of the date of publication. The DOI minted by Zenudo for the initial release at publication is listed in the key resources table.
- Any additional information required to reanalyze the data reported in this paper is available from the lead contact upon request.

EXPERIMENTAL MODEL AND SUBJECT DETAILS

Mouse models and animal ethics statement

All studies were approved by the National Cancer Institute-Frederick Animal Care and Use Committee. NCI-Frederick is accredited by AAALAC International and follows the Public Health Service Policy for the Care and Use of Laboratory Animals. Animal care was provided in accordance with the procedures outlined in the "Guide for Care and Use of Laboratory Animals (National Research Council; 1996; National Academy Press; Washington, D.C.). C57BL/6, BALB/c or *Rag-1* ko (B6.129S7-Rag1tm1Mom/J) female mice, 6–8 weeks of age, were used. For the orthotopic mouse EO771 or 4T1 breast model, cells were purchased from CH3 BioSystems or ATCC, respectively. KPC cells were kindly provided from Dr. Kozlov, Center for Advanced Preclinical Research, Frederick National Laboratory for Cancer Research. Cell lines were cultured in complete RPMI 1640 medium supplemented with 10% fetal bovine serum, 100 IU/mL Penicillin and 100 μg/mL Streptomycin. The cells were resuspended in PBS. Matrigel (Corning Inc.), an extract of basement membrane proteins, was added at 1:3 dilution to facilitate the inoculation process.[115] Cells ($3x10^5$) were orthotopically inoculated at the fourth mammary fat pad of mice and the tumor size was measured using a digital caliper. Tumor volume (mm^3) was calculated by the following equation: $L*W*H*\pi/6$.

Immunotherapy of EO771 or 4T1 tumor-bearing mice

Treatment was initiated when tumors reached ~20 mm^3. Animals were treated with hetIL-15,[41,43] which is a heterodimer comprising the IL-15 chain and soluble extracellular portion of IL-15 Receptor alpha chain. In some experiments, the hetIL-15Fc molecule was used, which is a fusion of hetIL-15 to the Fc fragment of human immunoglobulin G1 (IgG1), with similar results. hetIL-15 was administered in Matrigel (Corning Inc.), used in 1:4 dilution, every 4 days peritumorally at 5μg/mouse in PBS. Quizartinib (AC220, LC Laboratories) was administered by i.p. injections, every three days at 5 mg/kg in DMSO/PBS. In the survival studies, mice were sacrificed when the primary tumor reached a 2cm diameter or any other humane endpoints listed in the ACUC-approved animal protocol, such as 20% weight loss or acute morbidity.

NK cell depletion *in vivo*

EO771 tumor-bearing C57BL/6 mice were treated locoregionally with vehicle (control) or hetIL-15. For NK cell depletion, mice received 100μg of anti-NK1.1(α-NK1.1) mAb (clone PK13) or control IgG2a (BioXCell) delivered by intraperitoneal injection. Anti-NK1.1 or isotype was administered through intraperitoneal (i.p.) injection for four consecutive days before the inoculation of murine EO771 cells. Thereafter, α-NK1.1 mAb or IgG2a were injected every four days for the remainder of the experiment. Depletion of NK cells were confirmed through flow cytometry analysis of spleen and was consistently >95%.

Adoptive cell transfer

Recipient naive mice were challenged with 3×10^5 EO771 cells on day 0 and 6 days later the mice were irradiated with 600cGy (whole body irradiation; X-ray source, 1.29 Gy/minute, 137-cesium chloride irradiator). Eight days after tumor challenge, $CD8^+$T cells from spleen of naive or hetIL-15 treated mice rechallenged with EO771 tumor cells were injected into the

EO771 tumor-bearing mice. Recipient mice were boosted with hetIL-15 i.p. injections (5μg/dose/mouse) every 3 days until the end point.

Rechallenge experiments

C57BL/6 mice were inoculated with 3×10^5 EO771 cells. When palpable tumor had formed 7 days later, mice were treated with hetIL-15 injections, as described in the figure legends. On day 68, long-term surviving tumor-free mice were rechallenged with 5×10^4 EO771 cells. The mice remained tumor-free after the first rechallenge and on day 158, the mice were rechallenged again for a second time with 5×10^4 EO771 cells (fourth right mammary pad) and by injection of 5×10^4 KPC cells (third left mammary pad). Growth of individual EO771 and KPC tumors were monitored from the day of the second rechallenge until the end point.

METHOD DETAILS

Histology and immunohistochemistry staining

Tissue samples, including tumors, were fixed in 10% neutral buffered formalin (NBF, Sigma) then routinely processed and paraffin embedded. Tumor and lung sections were dewaxed and rehydrated and then were stained with hematoxylin and eosin (H&E). For immunohistochemistry, sections were antigen-retrieved with heat-induced or enzymatic method. Peroxidase activity was blocked using 1.5% hydrogen peroxide. Sections were blocked with different blocking protocols, depending on the antibody. Staining was performed using the following anti–mouse antibodies: anti-CD8a (clone 4SM15; eBioscience) and NK1.1 (clone E6Y9G; BD Biosciences). Polymer-based detection kit, which consists of horseradish peroxidase–conjugated polymers was used for the detection.

Splenic CD8a$^+$T cells isolation

Single-cell suspension of murine splenocytes were collected through a 100 μm cell strainer. The CD8a$^+$T cells isolation Kit (Miltenyi Biotec Inc.) was used for the isolation, according to the manufacturer protocol. Cells were isolated through negative selection using AutoMACS Pro Separator (Miltenyi Biotec Inc.).

Tumor-infiltrating CD11c$^+$ cell isolation

EO771 tumors from control and hetIL-15 treated animals were enzymatically digested using the tumor dissociation kit (Miltenyi Biotec Inc.) and mechanically dissociated using the GentleMACS Dissociator (Miltenyi Biotec Inc.). Tissues were passed through 100 μm cell strainers (Falcon) and washed with PBS before proceeding to the isolation step. The CD11c$^+$ cells isolation Kit (Miltenyi Biotec Inc.) was used, according to the manufacturer protocol. Cells were isolated through positive selection using AutoMACS Pro Separator (Miltenyi Biotec Inc.).

Flow cytometry

At necropsy, tumors and dLNs were processed for flow cytometric analysis. All tumors were weighed before the start of the process. To generate single cell suspensions, tumors were enzymatically digested using the tumor dissociation kit (Miltenyi Biotec Inc.) and mechanically dissociated using the GentleMACS Dissociator (Miltenyi Biotec Inc.). Tissues were passed through a 100 μm cell strainer (Falcon) and washed with PBS before proceeding with antibody mediated staining. dLNs were dissociated using a 100 μm cell strainer and washed with PBS. Surface staining was performed using the following anti–mouse antibodies: CD45 (clone 30-F11), CD3 (clone 145-2C11), CD8a (clone 53–6.6), CD19 (clone 1D3), NK1.1 (clone PK136), B220 (clone RA3-6B2), XCR1 (clone ZET), MHCII (clone M5/114.15.2), CD11c (clone N418), CD24a (clone M1/69), CD64 (clone X55-5/7.1), F4/80 (clone BM8), CD103 (clone M290), CD11b (clone M1/70), CD172a (clone P84), Ly6C (clone HK1.4), TREM-1 (clone TR3MBL1), CD101 (clone Moushi101), CX3CR1 (clone SA011F11) and GP2 (clone 2F11-C3). For intracellular staining, cells were fixed and permeabilized using the Foxp3 staining buffer. Samples were stained with Ki67 (clone B56), Granzyme B (clone GB12), IRF8 (clone V3GYWCH) and IFN-γ (clone XMG1.2). The samples were acquired on a Fortessa (BD Biosciences) flow cytometer, and the data were analyzed using the FlowJo software (Tree Star, Ashland, OR, USA). t-SNE analysis was performed using the FlowJo t-SNE plugin.

Gene expression analysis by nCounter PanCancer Immune Profiling Panel

Tumors were mechanically disrupted in RLT buffer (QIAGEN), and RNA extraction was performed with RNeasy (QIAGEN) including on-column DNase I digestion, according to the manufacturer's instructions. nCounter PanCancer Immune Profiling Panel (NanoString Technologies) was used to monitor the expression of a panel of 770 genes related to immuno-oncology. The mRNA molecules were counted with the NanoString nCounter at the Laboratory of Molecular Technology Advanced Technology Program, Frederick National Laboratory. Analysis was performed with a workflow written in R and through a user interface developed on the Foundry Platform (NIH Integrated Data Analysis Platform, Palantir Technologies). Filtering was performed on raw reads to genes with low counts leaving 769 from the array. Log-transformed counts were quantile normalized and tested for differential expression with limma-voom.[116] Pathway enrichment analysis was performed with the Fisher's Exact Test using the GO database and the top 150 positively and negatively differentially expressed genes as defined by t-statistic (https://github.com/CCBR/l2p). Immune cell

populations were scored by taking the geometric mean expression of reference marker genes within each sample, with makers for cytotoxic and dendritic cells taken from Danaher et al.[114]

Bulk RNA sequencing

Tumor-infiltrating DC subpopulations (CD103$^+$cDC1, CD11b$^+$cDC2 and CD103^{int}CD11b$^+$DC) and macrophages were sorted on a BD FACSAria II. For each cell subset, 4,000–20,000 viable cells were sorted directly into RTL buffer, flash frozen and stored at −80°C until RNA extraction. RNA was isolated using RNeasy Mini Kit (Qiagen) and removal of genomic DNA (gDNA) was performed with the DNase I enzyme (Qiagen), according to manufacturer's recommendations. Library preparation was performed using NEBNext Ultra II Directional RNA Library Prep Kit. At least 100 million reads per sample were used following the standard operating procedure at the Sequencing Facility - Illumina (CCR). Preprocessing, alignment, and gene-wise quantification steps were performed using the CCBR Pipeliner (https://github.com/CCBR/Pipeliner) as implemented by NIH HPC Biowulf cluster (http://hpc.nih.gov). Downstream analysis and visualization were performed in R as implemented on the NIH Integrated Data Analysis Platform.

CITE- and single-cell RNA-sequencing

1-2 million isolated tumor-infiltrating CD11c$^+$ populations from control and hetIL15-treated EO771-tumor bearing mice were pelleted and resuspended into 50μL of labelling buffer (PBS +1% BSA). Fc receptors were blocked by adding TruStain FcX (BioLegend) to the cell suspension at a concentration of 1μg TruStain FcX per million cells, mixed by gentle pipetting and incubated at 4°C for 10 min. CD24a antibody (TotalSeq-B0212, clone 51/69) was prepared by centrifuging it at 14K rpm at 4°C for 10mins. Supernatant of the prepared antibody was added to the samples to a final concentration of 1μg of individual antibodies/million cells in a total volume of 100μL (volume was maintained using labelling mix). Cells were stained with antibody for 30 min at 4°C and then washed 3 times with 1.5mL of labelling buffer each. After washing, cells were resuspended in 1 mL of PBS +0.04% BSA and counted. Approximately 10,000 cells from every sample were then loaded on one channel of the 10X chip and GEMs (Gel Beads-in-emulsion) were generated using the 10X Genomics Chromium Controller. 3′ mRNA-seq gene expression libraries were then prepared using the Chromium Next GEM Single Cell 3' Reagent Kits v3.1. These libraries were pooled and first run on NextSeq500 as asymmetric paired-end run with a read length of 28bp for Read 1,55bp for Read 2, and 8bp for the sample index read. The data from this run was used to calculate the re-pooling ratios for better balancing of the libraries, and the new pool of the six gene expression libraries was sequenced on a NovaSeq SP (100 cycle) run as asymmetric paired-end run with a read length of 28bp for Read 1, 75bp for Read 2, and 8bp for the sample index read. The data from the two sequencing runs for gene expression libraries was pooled for the final analysis. Cellranger v4.0.0 count matrices were analyzed with a workflow written in R, through a user interface developed on the Foundry Platform (NIH Integrated Data Analysis Platform, Palantir Technologies). Quality control, normalization and variance stabilization (via SCTransform[117]), merging, and clustering was performed using Seurat v3.1.5. For CITE-seq, protein counts were normalized and scaled for comparison across RNA and protein. Cells were serially annotated with scRNA-seq reference datasets from Brown et al.[50] and our own bulk RNA-seq dataset from FACS-purified populations with SingleR v1.0.0.[118] Single-sample GSEA analysis was performed on cluster average gene expression using the GSVA v1.30.0 R package[110] against dendritic cell pathways extracted from all collections in MSigDB (v6.2).[111,112] Normalized enrichment scores were row scaled and plotted with heatmap v1.0.12. MSigDB dendritic cell pathways and Seurat clusters were clustered within the heatmap using Euclidean distances.

Multiplex RNA *in situ* hybridization staining

CD24a, *Mgl2*, and *Ccl17* expression was detected by staining 5μm FFPE tissue sections with RNAscope 2.5 LS Probe –Mm-CD24a-C1 (ACD, Cat# 432698), RNAscope 2.5 LS Probe –Mm-Mgl2-O1 (ACD, Cat# 822908-C2), RNAscope 2.5 LS Probe –Mm-Ccl17-C3 (ACD, Cat# 428498-C3), and the RNAscope LS Multiplex Fluorescent Assay (ACD, Cat# 322800) using the Bond RX auto-stainer (Leica Biosystems) with a tissue pretreatment of 15 min at 95°C with Bond Epitope Retrieval Solution 2 (Leica Biosystems), 15 min of Protease III (ACD, Cat#322340) at 40°C, and 1:750 dilution of TSA-Cyanine 5 Plus, TSA-Fluorescein Plus and TSA-Cyanine 3 Plus (AKOYA), respectively. The RNAscope 3-plex LS Multiplex Negative Control Probe (Bacillus subtilis dihydrodipicolinate reductase (*dapB*) gene in channels C1, C2, and C3, Cat# 320878) was used as a negative control. The RNAscope LS 2.5 3-plex Positive Control Probe-Hs was used as a technical control to ensure the RNA quality of tissue sections was suitable for staining. Slides were digitally imaged using an Aperio ScanScope FL Scanner (Leica Biosystems).

Direct co-culture of DCs with CD8$^+$ T cells

Sorted tumor-infiltrating CD103$^+$cDC1s, CD11b$^+$cDC2s or CD103^{int}CD11b$^+$DC were co-cultured with isolated splenic CD8$^+$T cells from naive mice (ratio DC: CD8$^+$T cells, 1:10) in RPMI1640 supplemented with 10% fetal bovine serum, 100 IU/mL Penicillin and 100 μg/mL Streptomycin, GM-CSF (100 U/mL) and IL-2 (30IU/mL). After 24hrs incubation, the cells were harvested, washed, and analyzed by flow cytometry to determine IFN-γ expression.

QUANTIFICATION AND STATISTICAL ANALYSIS

GraphPad Prism 9.4.1 (San Diego, CA, USA) was used for data analysis and statistical significance was determined by unpaired non-parametric (Mann Whitney) or two-way analysis of variance (ANOVA) or mixed-effects analysis with Holm-Sidak's multiple comparisons test or using the MAST algorithm.[113] Survival was represented with Kaplan-Meier curves and the log rank (Mantel-Cox) test was applied for statistical survival analysis. Statistically significant differences are indicated in figures and error bars in figures indicate the standard error of the mean (SEM) for the number of animals, as indicated in the figure. Pearson correlation was used to test the relationship between cell count and tumor volume. For Nanostring analysis, p values were adjusted via the Benjamini-Hochberg Procedure to minimize the false discovery rate.[119]

Cell Reports, Volume *42*

Supplemental information

Tumor eradication by hetIL-15 locoregional therapy correlates with an induced intratumoral $CD103^{int}CD11b^{+}$ dendritic cell population

Dimitris Stellas, Sevasti Karaliota, Vasiliki Stravokefalou, Matthew Angel, Bethany A. Nagy, Katherine C. Goldfarbmuren, Cristina Bergamaschi, Barbara K. Felber, and George N. Pavlakis

Supplemental Information

Supplemental information includes 9 Supplemental figures

Figure S1 (related to Fig.1)

Figure S2 (related to Fig.2)

Figure S3 (related to Fig.3)

Figure S4 (related to Fig.4)

Figure S5 (related to Fig.5)

Figure S6 (related to Fig.5)

Figure S7 (related to Fig.6)

Figure S8 (related to Fig.6)

Figure S9 (related to Fig.6)

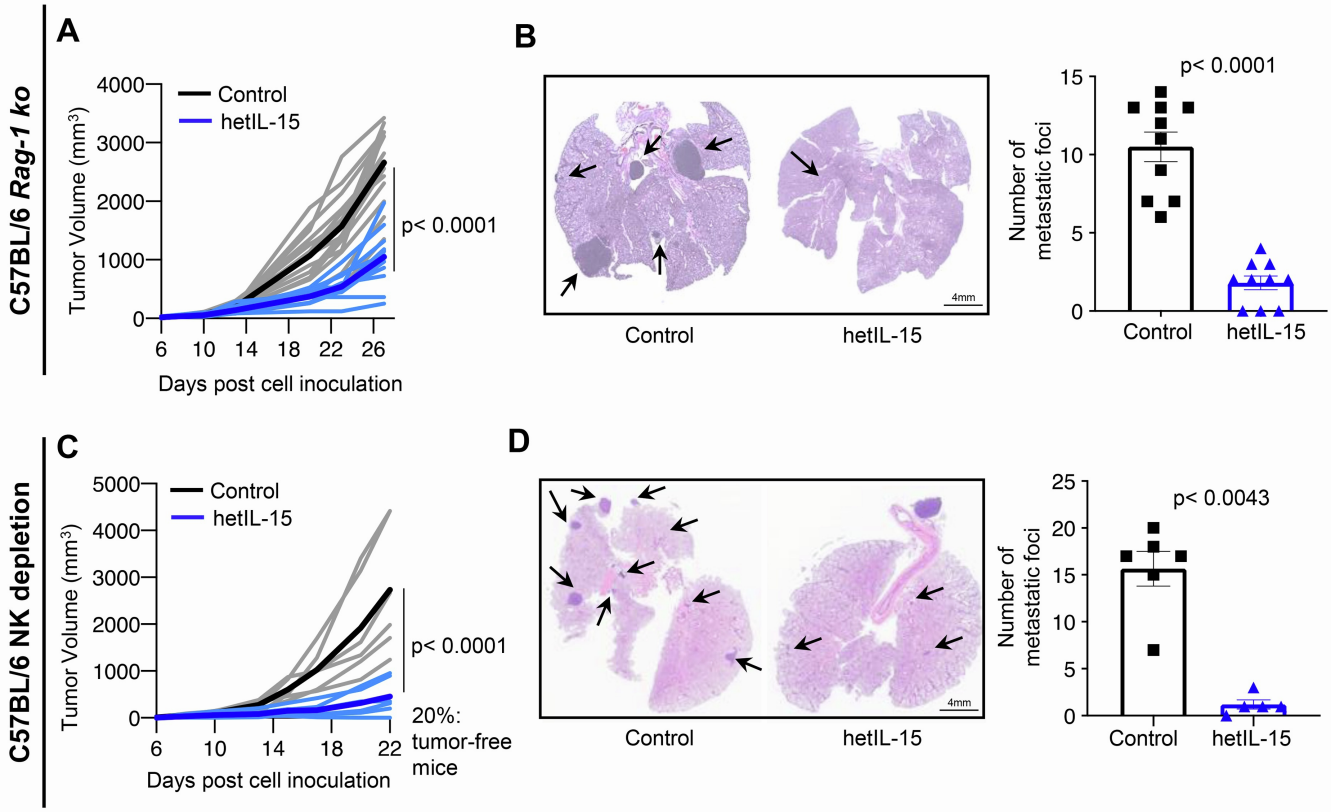

Figure S1. Comparison of EO771 tumor growth and metastasis in orthotopic mouse models of different immunological backgrounds. Related to Figure 1. (A, C) Tumor growth curves (bold lines represent average values) of C57BL/6 *Rag-1* ko (A) or C57BL/6 NK cells depleted (C) mice. hetIL-15 (5µg/dose/mouse) was injected every 4 days for a total of 6 (A) or 5 (C) doses. Injections of anti-NK1.1 mAb or IgG2a (100µg/dose/mouse, i.p.) were performed as described in Methods Details section. (B, D) *H&E* representative staining images (left panel) and number of metastatic foci (right panel) of EO771 lung metastases in control or hetIL-15 treated C57BL/6 *Rag-1* ko (B) or C57BL/6 NK depleted (D) mice. Arrows in images indicate the metastatic foci. Scale bar = 4mm. Data represented as mean ±SEM are from one experiment with n= 13-15 (A) and n= 10 (B) mice per group or 5-6 mice per group (C and D). Statistical significance was calculated by 2-way ANOVA (A and C) and by Mann-Whitney U test (B and D).

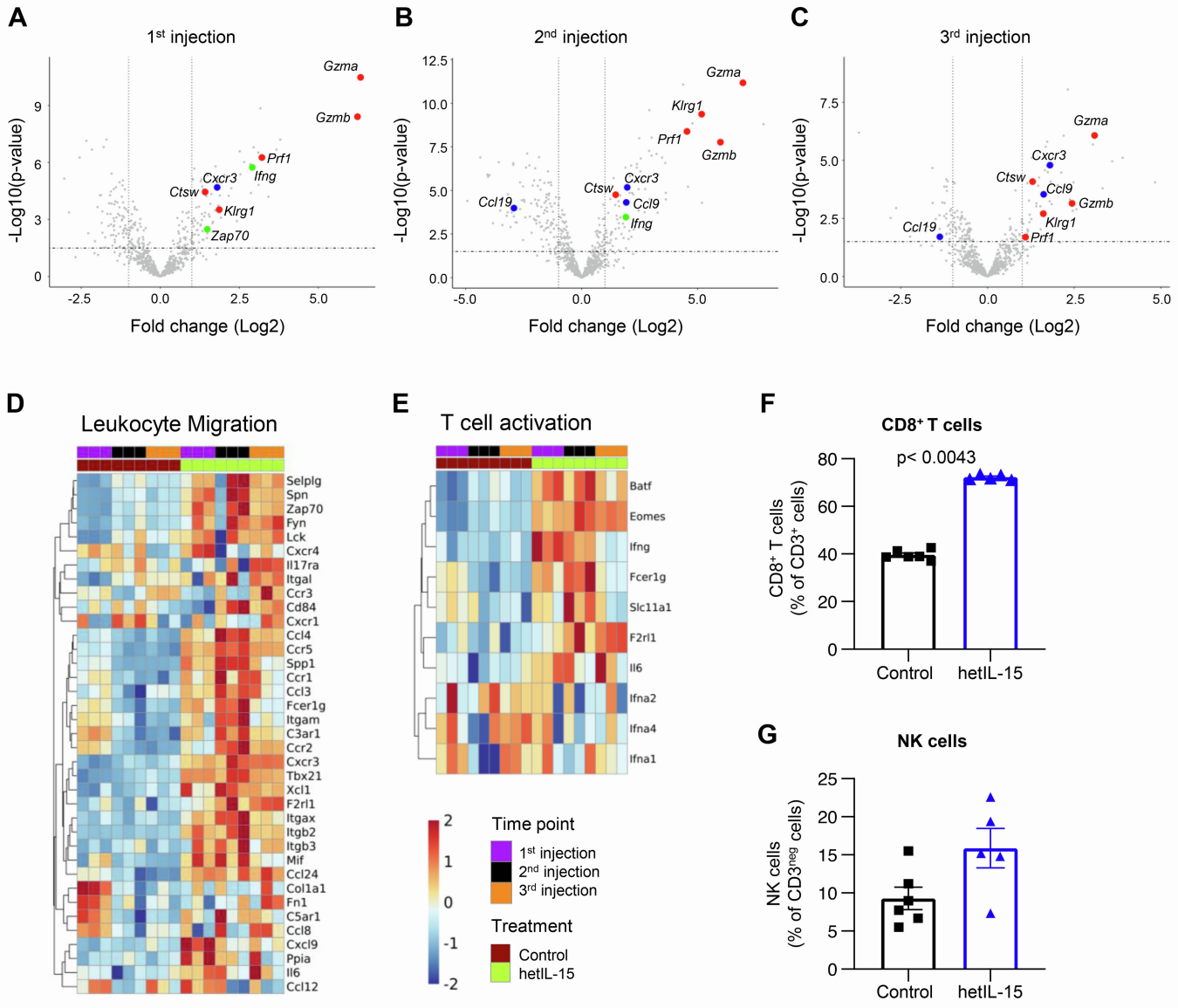

Figure S2. hetIL-15 treatment altered gene expression of the draining lymph nodes. Related to Figure 2. (A-C) Volcano plots depict differentially expressed genes in the two groups after the 1st, 2nd and 3rd locoregional hetIL-15 injection. Dashed line represents adjusted p-value=0.05 and dotted lines represent log2(FC)=1 and log2(FC)=-1. The genes marked in red, green and blue are associated with T and NK cell cytotoxicity, enhanced T cell activation/TCR signaling and lymphocyte migration, respectively. Dashed line represents Benjamini-Hochberg adjusted p-value=0.05 and dotted lines represent log2(FC)=1 and log2(FC)=-1. (D, E) Heatmaps of differentially expressed genes in the lymphocyte migration and T cell activation pathways. (F, G) dLNs were also analyzed by flow cytometry to determine the percentage of: $CD8^+$T (F) and NK (G) cells. The analysis was performed 48hrs post the 3rd hetIL-15 injection. Data are from one experiment with 5-6 mice per group, shown as mean ±SEM. Statistical significance was calculated using Mann-Whitney U test.

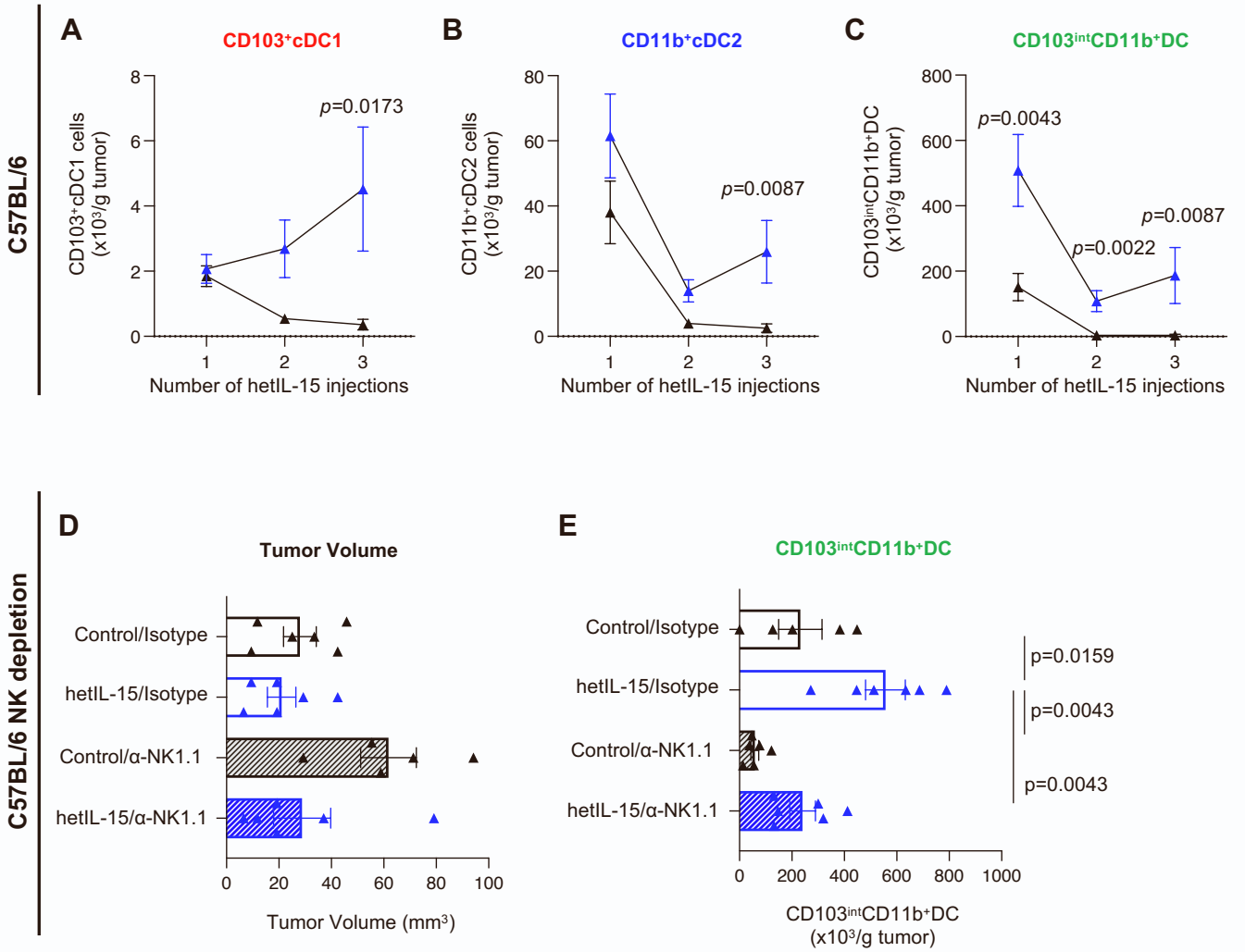

Figure S3. CD103^{int}CD11b^{+}DCs are present in tumors of hetIL-15 treated mice, as early as 48h after the 1st hetIL-15 injection and their accumulation is NK cell-dependent. Related to Figure 3. (A-C) Flow cytometric analysis of tumor-infiltrating CD103^{+}cDC1 (A), CD11b^{+}cDC2 (B) and CD103^{int}CD11b^{+}DC (C) populations by flow cytometric analysis in controls and hetIL-15 treated mice, per time point. On day -1, C57BL/6 mice were inoculated with 3×10^{5} EO771 cells orthotopically in the 4th mammary pad. Mice with palpable tumors were distributed in different groups 7 days later and treated locoregionally with hetIL-15 injections (5μg/dose/mouse) in the mammary fat pad in the vicinity of the tumor every 4 days. The analysis was conducted 48hrs post the 1st, 2nd and 3rd hetIL-15 injection. Data are from one experiment with 5-6 mice per group for each time point and shown as mean ±SEM. P values show the significance of compared to the untreated group and were calculated by Mann-Whitney U test. (D-E) Tumor volume (mm^{3}) (D) and flow cytometric analysis of intratumoral CD103^{int}CD11b^{+}DCs (E) of controls and hetIL-15 treated C57BL/6 NK cell-depleted mice. Injections of anti-NK1.1 mAb or IgG2a (100μg/dose/mouse, i.p.) were performed. The analysis was performed 48hrs post the 1st hetIL-15 injection. Data are from one experiment (n=5-6 mice/group) and shown as mean ±SEM. Statistical significance was calculated by Mann-Whitney U test.

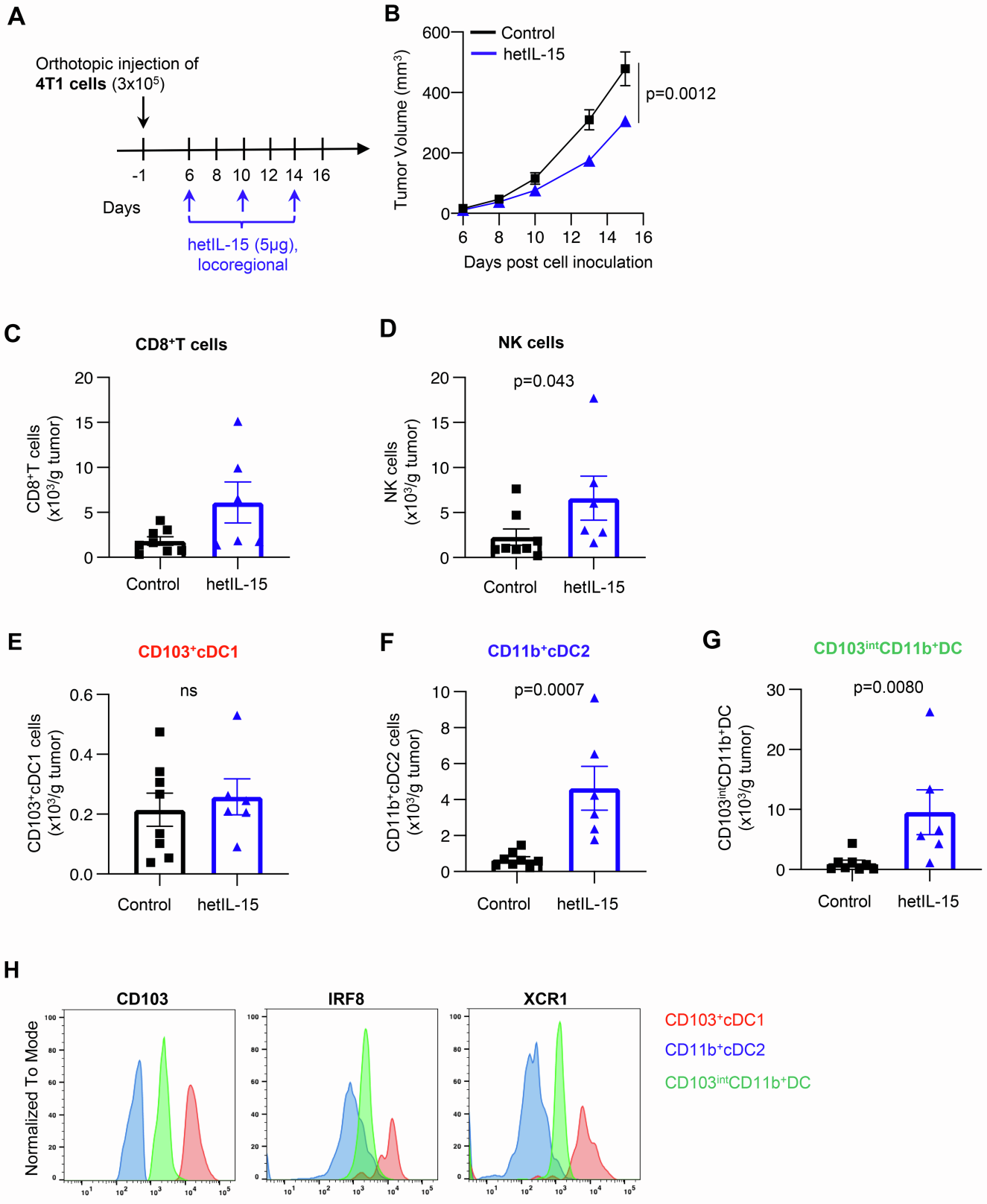
A
Orthotopic injection of
4T1 cells (3x10^5)
-1
6
8
10
12
14
16
Days
hetIL-15 (5µg),
locoregional
B
Control
hetIL-15
Tumor Volume (mm^3)
600
400
200
0
p=0.0012
6
8
10
12
14
16
Days post cell inoculation
C
CD8+T cells
CD8+T cells
(x10^3/g tumor)
20
15
10
5
0
Control
hetIL-15
D
NK cells
p=0.043
NK cells
(x10^3/g tumor)
E
CD103+cDC1
ns
CD103+cDC1 cells
(x10^3/g tumor)
0.6
0.4
0.2
0.0
F
CD11b+cDC2
p=0.0007
CD11b+cDC2 cells
(x10^3/g tumor)
10
8
6
4
2
G
CD103intCD11b+DC
p=0.0080
CD103intCD11b+DC
(x10^3/g tumor)
30
20
10
H
CD103
IRF8
XCR1
Normalized To Mode
CD103+cDC1
CD11b+cDC2
CD103intCD11b+DC

Figure S4. hetIL-15 associated CD103^{int}CD11b^{+}DC population is present in 4T1 orthotopic tumors, upon hetIL-15 treatment. Related to Figure 4. Female Balb/c mice were implanted with 3×10^5 4T1 cells orthotopically into the 4th inguinal mammary fat pad and when palpable tumor had formed, the mice were treated with hetIL-15 or vehicle (control). (A) Treatment schedule. Injections of hetIL-15 (5μg/dose/mouse) were performed every 4 days for a total of 3 doses. (B) Tumor growth was monitored overtime. Data are from one experiment with 8-12 mice per group, shown as mean ±SEM. 4T1 tumor-bearing mice were sacrificed at day 16 after treatment with either saline or hetIL-15 (48hrs after the 3rd administration). Statistical significance was determined by mixed-effects analysis. (C-G) Tumor immune infiltrates were analyzed by flow cytometry to determine the absolute number of the cells per gram of tissue of: CD8^{+} T cells (C), NK cells (D) and CD103^{+}cDC1 (E), CD11b^{+}cDC2 (F) and CD103^{int}CD11b^{+}DC (G) populations. Data are from one experiment with 6-8 mice per group, plotted as mean ±SEM. Statistical significance was calculated using Mann-Whitney U test. (H) Flow cytometric analysis of CD103, IRF8 and XCR1 expression. Histogram overlays show the expression of CD103, IRF8 and XCR1 by intratumoral CD103^{+}cDC1 (red), CD11b^{+}cDC2 (blue) and CD103^{int}CD11b^{+}DC (green) populations from a representative hetIL-15 treated mouse. The analysis in panels C to H was performed 48hrs post the 3rd hetIL-15 injection.

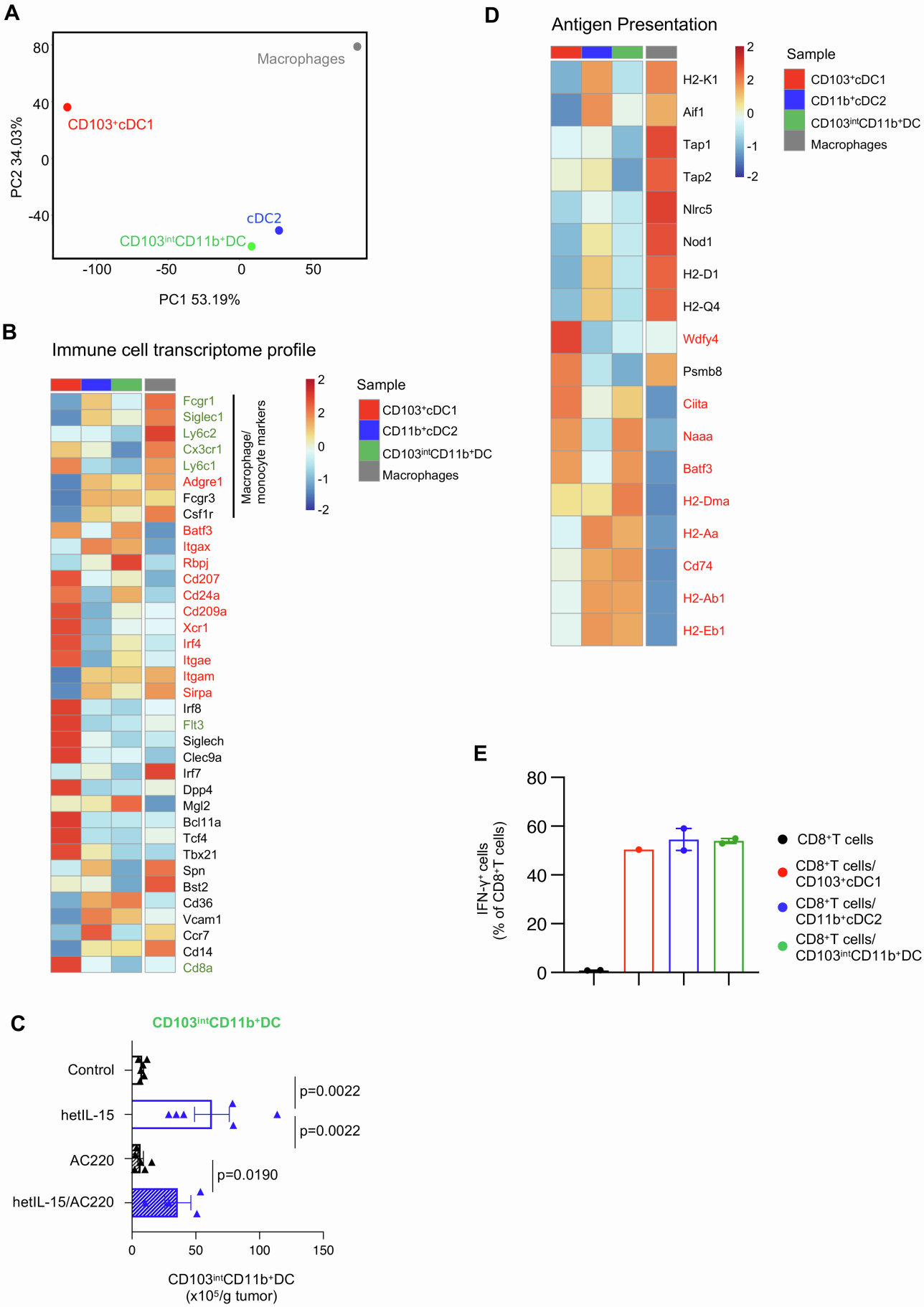
A
Macrophages
CD103⁺cDC1
cDC2
CD103ᵢₙₜCD11b⁺DC
PC2 34.03%
PC1 53.19%
B
Immune cell transcriptome profile
Macrophage/ monocyte markers
Fcgr1
Siglec1
Ly6c2
Cx3cr1
Ly6c1
Adgre1
Fcgr3
Csf1r
Batf3
Itgax
Rbpj
Cd207
Cd24a
Cd209a
Xcr1
Irf4
Itgae
Itgam
Sirpa
Irf8
Flt3
Siglech
Clec9a
Irf7
Dpp4
Mgl2
Bcl11a
Tcf4
Tbx21
Spn
Bst2
Cd36
Vcam1
Ccr7
Cd14
Cd8a
Sample
CD103⁺cDC1
CD11b⁺cDC2
CD103ᵢₙₜCD11b⁺DC
Macrophages
D
Antigen Presentation
H2-K1
Aif1
Tap1
Tap2
Nlrc5
Nod1
H2-D1
H2-Q4
Wdfy4
Psmb8
Ciita
Naaa
Batf3
H2-Dma
H2-Aa
Cd74
H2-Ab1
H2-Eb1
Sample
CD103⁺cDC1
CD11b⁺cDC2
CD103ᵢₙₜCD11b⁺DC
Macrophages
E
IFN-γ⁺ cells (% of CD8⁺T cells)
CD8⁺T cells
CD8⁺T cells/ CD103⁺cDC1
CD8⁺T cells/ CD11b⁺cDC2
CD8⁺T cells/ CD103ᵢₙₜCD11b⁺DC
C
CD103ᵢₙₜCD11b⁺DC
Control
hetIL-15
AC220
hetIL-15/AC220
p=0.0022
p=0.0022
p=0.0190
CD103ᵢₙₜCD11b⁺DC (x10⁵/g tumor)

Figure S5. Transcriptional analysis highlights distinct profile of tumor CD103^{int}CD11b^{+}DC. Related to Figure 5. Tumor-infiltrating DC subpopulations (CD103^{+}cDC1, CD11b^{+}cDC2 and CD103^{int}CD11b^{+}DC) and macrophages were sorted 48hrs after the 3rd hetIL-15 injection, based on the gating strategy shown in Figure 3B. RNA isolation and bulk RNA-seq analysis was performed to the sorted populations. (A) PCA of CD103^{+}cDC1, CD11b^{+}cDC2, CD103^{int}CD11b^{+}DC populations and macrophages based on RNA-seq global transcriptional profiles. (B) Heat map of log2-transformed expression from RNA-seq across populations for DC canonical markers[50] as well as from macrophage/monocyte markers. Red and green gene names indicate genes that are upregulated and downregulated, respectively. (C) Flow cytometric analysis of intratumoral CD103^{int}CD11b^{+}DC population in control, hetIL-15 and/or AC220 treated mice. On day -1, C57BL/6 mice were inoculated with 3×10^{5} EO771 cells (s.c in the 4th mammary pad). Mice with palpable tumors were distributed in different groups 7 days later and treated with 3 locoregional hetIL-15 injections (3μg/mouse/dose) every 4 days and AC220 (i.p, 5mg/kg) every 3 days. Data in graph are from one experiment (n=4-6), given as absolute numbers of cells per gram of tissue and represented as mean ±SEM. Statistical significance was determined by Mann-Whitney U test. (D) Heatmap of genes in the antigen presentation pathway[51] among DC cell subsets and macrophages. Red gene names indicate upregulated genes. (E) IFN-γ production in isolated splenic CD8^{+}T cells from naïve mice upon *ex vivo* co-culture with sorted tumor-infiltrating CD103^{+}cDC1, CD11b^{+}cDC or CD103^{int}CD11b^{+}DC populations, 48hrs after the 3rd hetIL-15 injection. Data shown are from one experiment presented as mean ±SEM.

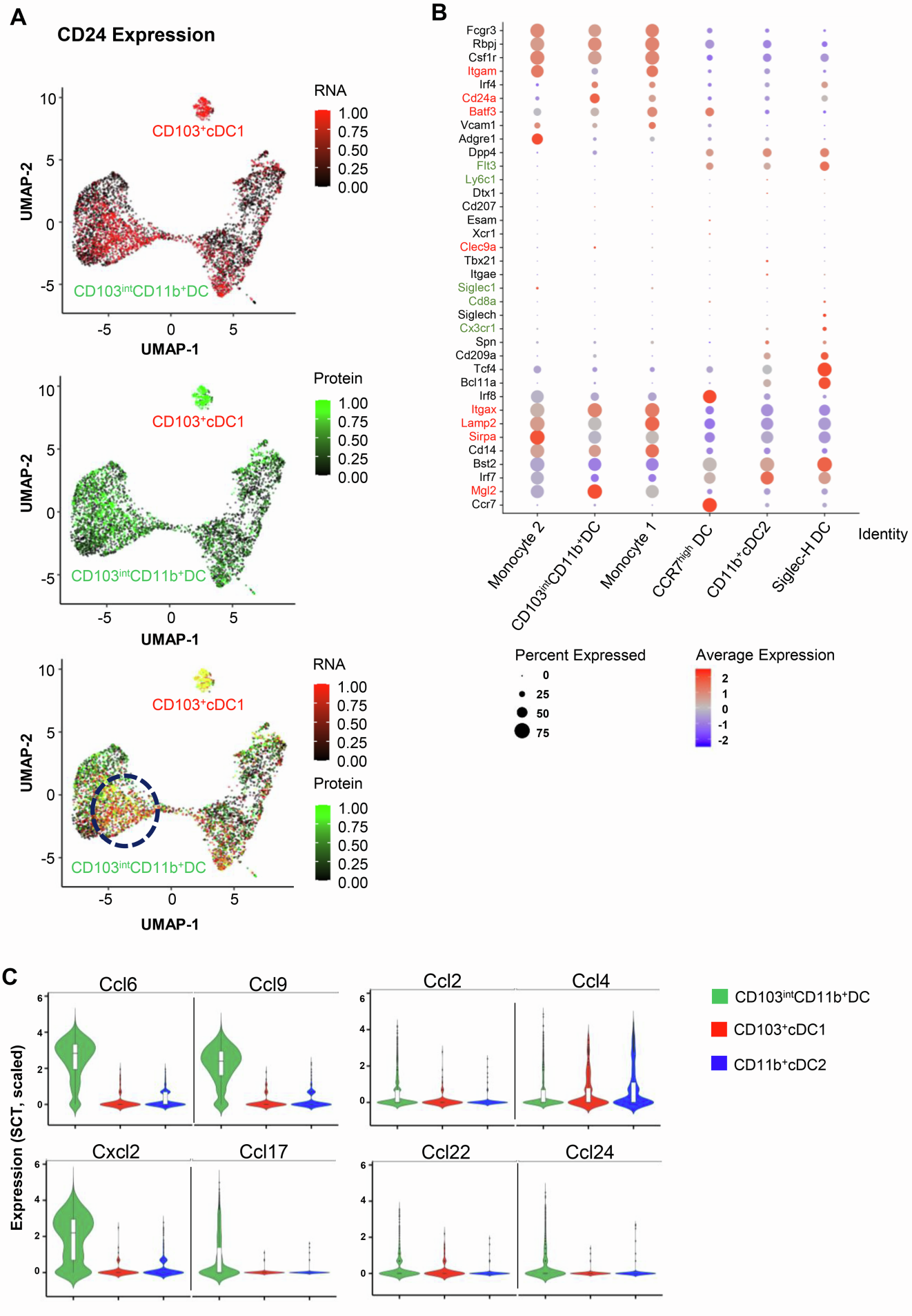
A
CD24 Expression
RNA
Protein
CD103+cDC1
CD103intCD11b+DC
UMAP-1
UMAP-2
B
Fcgr3
Rbpj
Csf1r
Itgam
Irf4
Cd24a
Batf3
Vcam1
Adgre1
Dpp4
Flt3
Ly6c1
Dtx1
Cd207
Esam
Xcr1
Clec9a
Tbx21
Itgae
Siglec1
Cd8a
Siglech
Cx3cr1
Spn
Cd209a
Tcf4
Bcl11a
Irf8
Itgax
Lamp2
Sirpa
Cd14
Bst2
Irf7
Mgl2
Ccr7
Monocyte 2
CD103intCD11b+DC
Monocyte 1
CCR7high DC
CD11b+cDC2
Siglec-H DC
Identity
Percent Expressed
Average Expression
C
Ccl6
Ccl9
Ccl2
Ccl4
Cxcl2
Ccl17
Ccl22
Ccl24
Expression (SCT, scaled)
CD103intCD11b+DC
CD103+cDC1
CD11b+cDC2

Figure S6. Sc-RNA sequence analysis reveals unique profile of the hetIL-15 associated CD103^{int}CD11b^{+}DC population. Related to Figure 5. Isolated tumor-infiltrating CD11c^{+} populations from control and hetIL15-treated EO771-tumor bearing mice were processed into single-cell suspension, 48hrs after the 3rd hetIL-15 injection. (A) CD24 expression in scRNA-seq SCTransformed log normalized RNA (red, top panel) and CITE-seq scaled normalized protein (green, middle panel) assays were each quantile filtered and scaled from 0 to 1. Overlay of red and green appears yellow, illustrating co-detection of both mRNA and protein for CD24 (lower panel), which is largely present in CD103^{+}cDC1 and novel CD103^{int}CD11b^{+}DC populations (highlighted). (B) Average expression bubble plot of genes in the canonical DC marker[50] gene set as well as from macrophage/monocyte markers, among clusters in the scRNA-seq dataset colored by average gene expression of SCTransformed scaled counts. Due to high gene expression in CD103^{+}cDC1, this cluster was removed to explore smaller differences between the remaining clusters. (C) Gene expression levels of chemokines are shown for CD103^{+}cDC1, CD11b^{+} cDC2 and CD103^{int}CD11b^{+} DC clusters. P-values, determined using the MAST algorithm, were < 0.001 for differences between CD103^{int}CD11b^{+}DC and both CD103^{+}cDC1 and CD11b^{+}cDC2 for all cytokines listed with the exception of *Ccl2* which was only significant different for CD103^{int}CD11b^{+}DC vs CD11b^{+}cDC2.

A

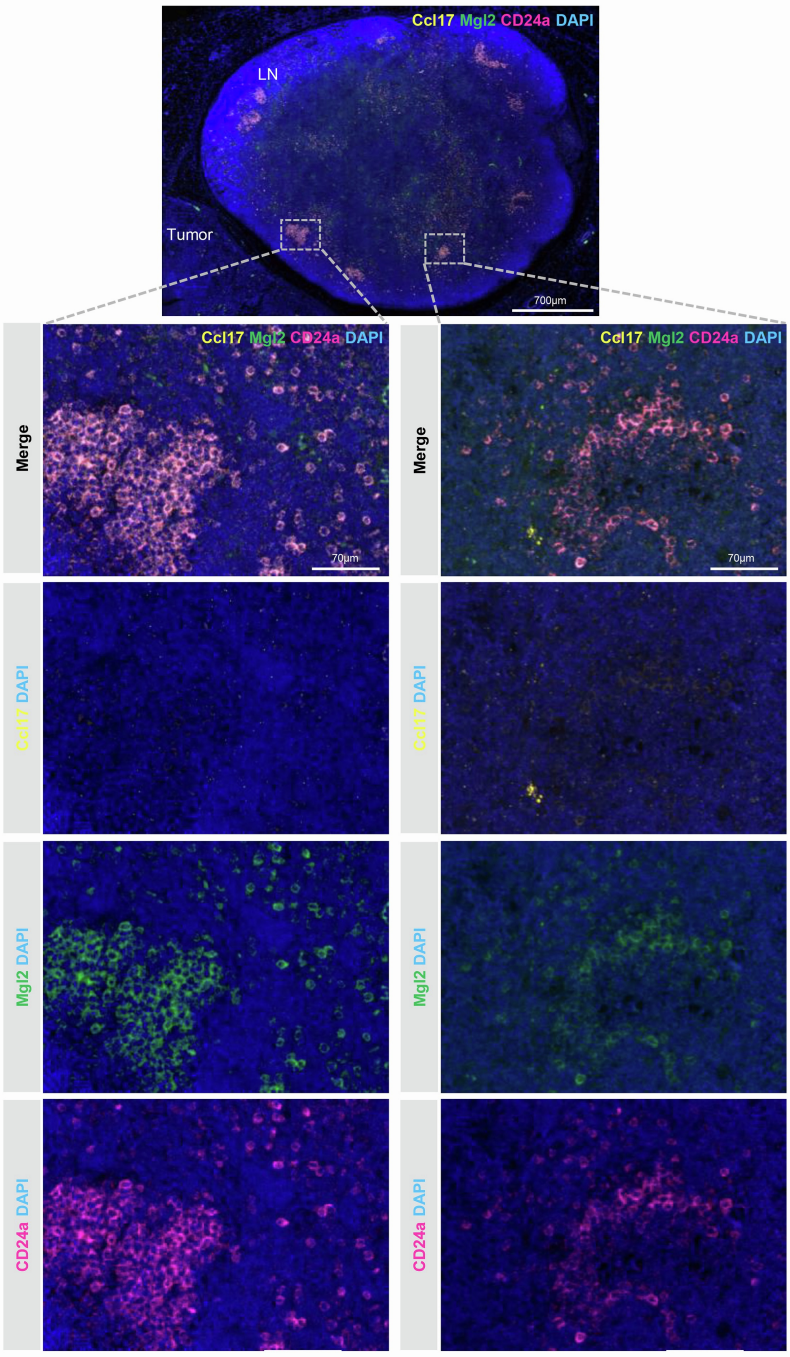
Ccl17 Mgl2 CD24a DAPI
LN
Tumor
700μm
Merge
Ccl17 Mgl2 CD24a DAPI
70μm
Merge
Ccl17 Mgl2 CD24a DAPI
70μm
Ccl17 DAPI
Ccl17 DAPI
Mgl2 DAPI
Mgl2 DAPI
CD24a DAPI
CD24a DAPI

B

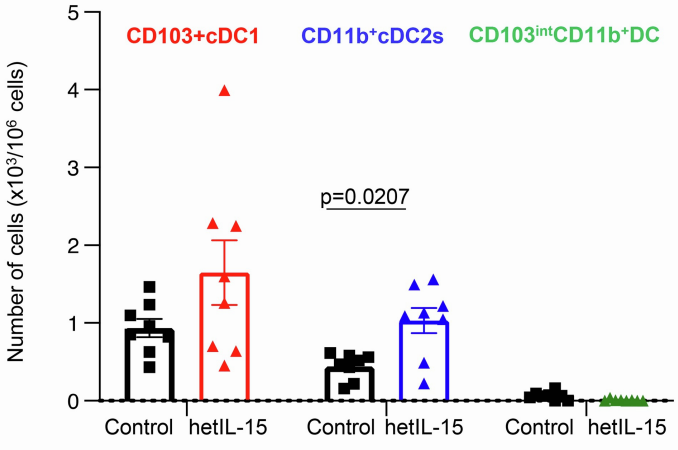
CD103+cDC1
CD11b+cDC2s
CD103intCD11b+DC
Number of cells (x10³/10⁶ cells)
5
4
3
2
1
0
p=0.0207
Control
hetIL-15
Control
hetIL-15
Control
hetIL-15

Figure S7. CD103^{int}CD11b^{+}DCs are not present in the dLNs EO771 cancer samples. Related to Figure 6. (A) Triple RNA in situ hybridization of EO771 tumor samples with dLNs verified the absence of the CD103^{int}CD11b^{+}DCs in the dLNs. Low-magnification image (700mm, upper panel) and 20x images (70mm; bottom) showing the expression of *Ccl17* (yellow), *Mgl2* (green) and *CD24a* (pink) mRNA in paraffin embedded tissue. Nuclear staining using DAPI (blue). Representative images from one experiment with 5 mice per group. (B) Flow cytometric analysis of CD103^{+}cDC1, CD11b^{+}cDC2 and CD103^{int}CD11b^{+}DC populations in dLNs of controls and hetIL-15 treated mice. Data shown are from one experiment (8 mice per group), shown as mean ±SEM and statistical significance was calculated using Mann-Whitney U test. The analysis of the samples was performed 48hrs post the 3rd hetIL-15 injection.

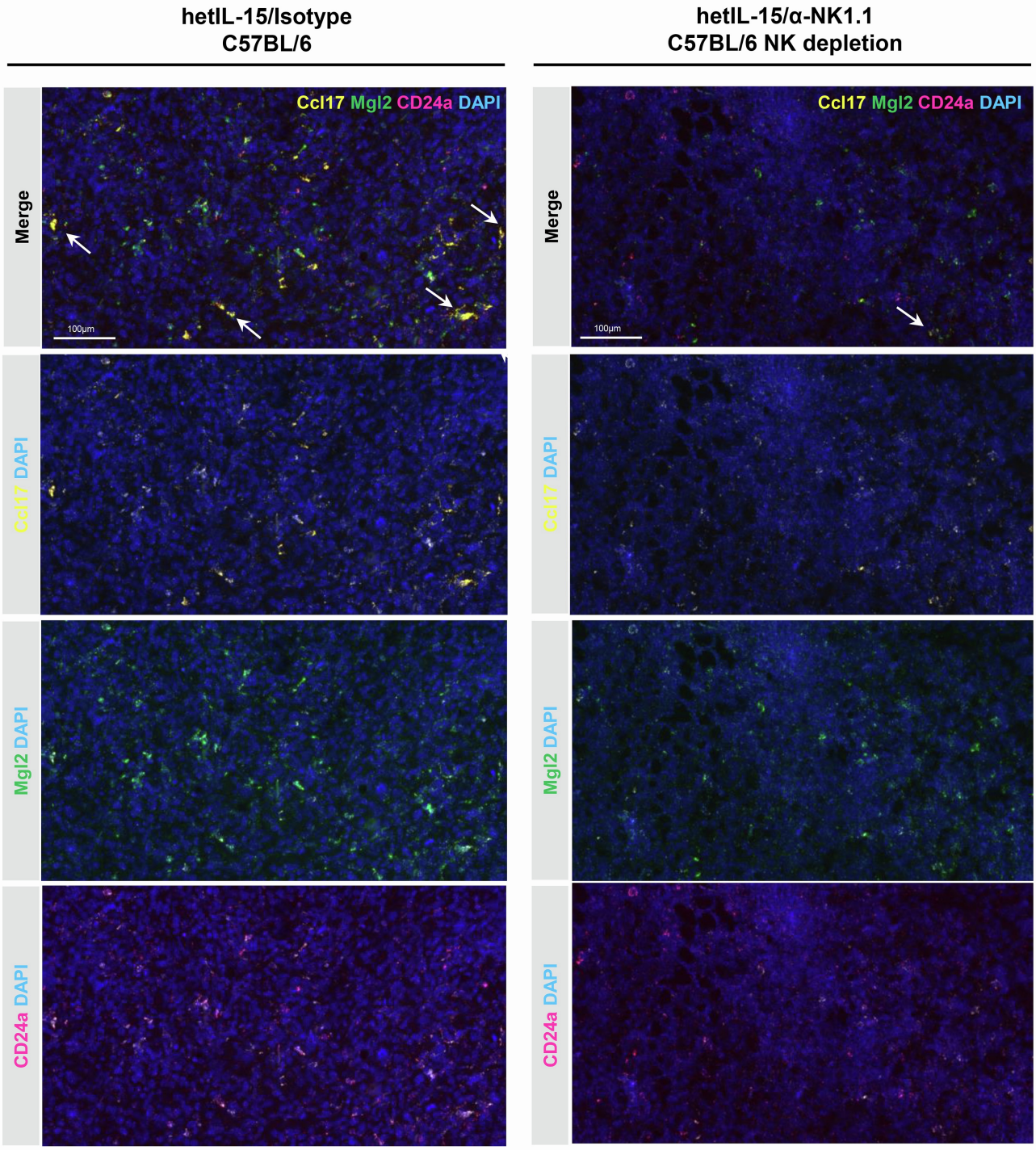

Figure S8. Tumor-infiltrating CD103^{int}CD11b^{+}DCs accumulation is NK cell-dependent. Related to Figure 6. Triple RNA in situ hybridization in EO771 tumor samples of hetIL-15 treated C57BL/6 (left panel) and C57BL/6 NK cell-depleted (right panel) mice, 48hrs after the 1st hetIL-15 injection. Injections of anti-NK1.1 mAb or IgG2a (100mg/dose/mouse, i.p.) were performed. Images show expression of *Ccl17* (yellow), *Mgl2* (green) and *CD24a* (pink) mRNA in paraffin embedded tissue. Nuclear staining using DAPI (blue). White arrows indicate the CD103^{int}CD11b^{+}DCs. Representative images from one experiment with 5 mice per group.

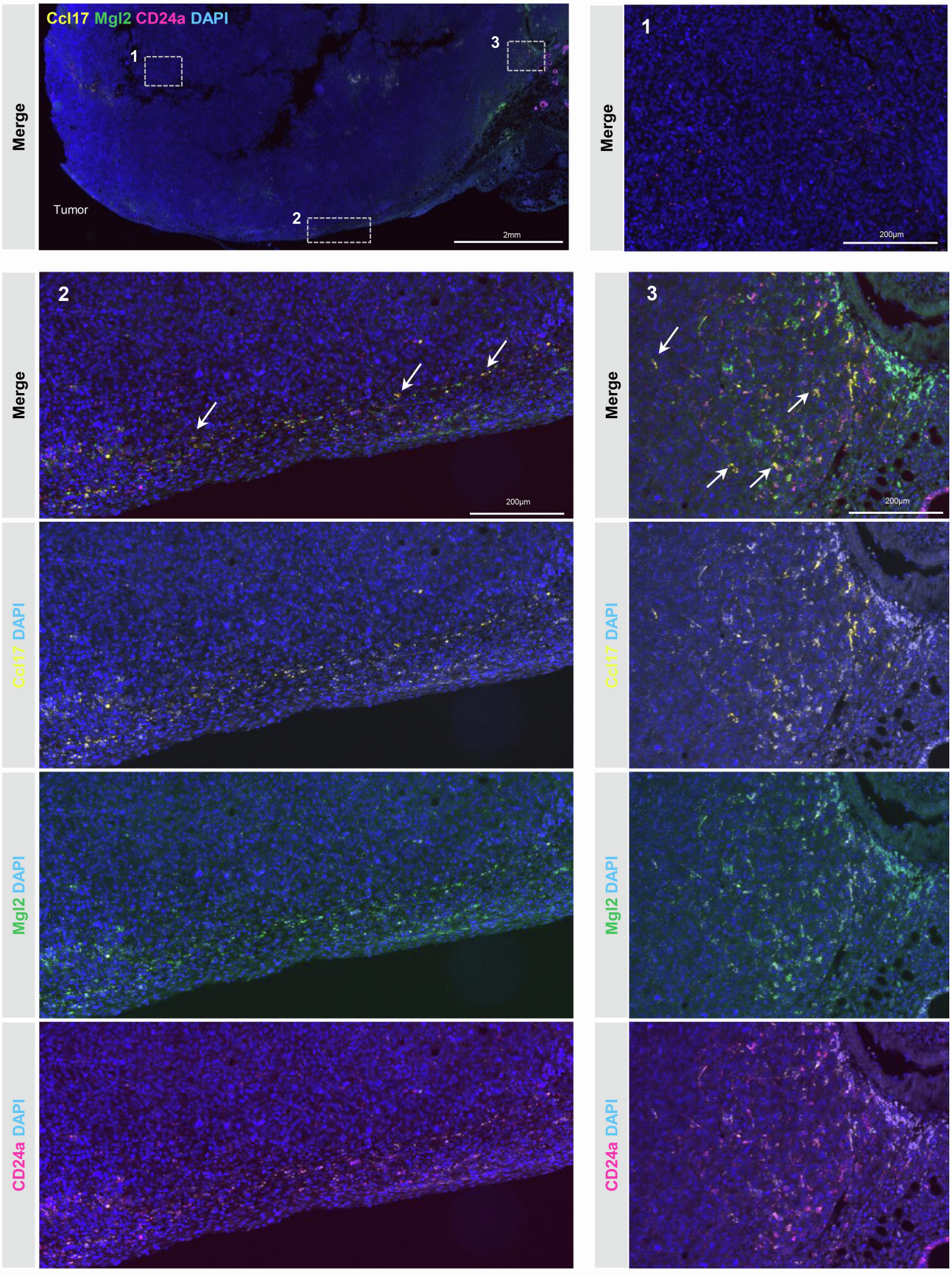
Merge
Ccl17 Mgl2 CD24a DAPI
1
2
3
Tumor
2mm
200μm
Ccl17 DAPI
Mgl2 DAPI
CD24a DAPI

Figure S9. CD103^{int}CD11b^{+}DCs are present in the tumors of the hetIL-15 treated C57BL/6 *Rag-1* ko mice but only in the periphery of the tumor. Related to Figure 6. Triple RNA in situ hybridization in paraffin embedded tissue of EO771 cancer samples from hetIL-15 treated C57BL/6 *Rag-1* ko mice, 48hrs after the 4th hetIL-15 injection. Upper panel showing low-magnification image of the tumor sample (2mm, left panel). Higher magnification representative images (55×, 200μm) of areas from the center (1) and from the periphery (2 and 3) of the tumor showing CD103^{int}CD11b^{+}DCs expressing *Ccl17* (yellow), *Mgl2* (green) and *CD24a* (pink) mRNA. Nuclear staining using DAPI (blue). White arrows indicate the CD103^{int}CD11b^{+}DCs. Representative images from one experiment with 5 mice per group.